Electronic and Thermal Response of Low-Electron-Density Drude Materials to Ultrafast Optical Illumination

Subhajit Sarkar⬚,*,† Ieng Wai Un,†,‡ and Yonatan Sivan⬚§

School of Electrical and Computer Engineering, Ben-Gurion University of the Negev and the Ilse Katz Center for Nanoscale Science and Technology, Ben-Gurion University of the Negev, Beer Sheva 84105, Israel

Many low-electron-density Drude (LEDD) materials such as transparent conductive oxides or nitrides have recently attracted interest as alternative plasmonic materials and extremely nonlinear thermal and optical materials. These materials attract research interest because they are CMOS compatible; hence, they can enable new functionalities within existing devices. However, the rapidly growing number of experimental studies has so far not been supported by a systematic theory of the electronic, thermal, and optical response of these materials. Here, we use the techniques previously derived in the context of noble metals to go beyond a simple electromagnetic modeling of LEDD materials and provide an electron-dynamics model for their electronic and thermal response. We find that the low electron density makes momentum conservation in electron-phonon interactions more important, more complex, and more sensitive to the temperatures compared with noble metals; moreover, we find that electron-electron interactions are becoming more effective due to the weaker screening. Most importantly, we show that the low electron density makes the electron heat capacity much smaller than in noble metals, such that the electrons in LEDD materials tend to heat up much more and cool down faster compared to noble metals. While here we focus on indium tin oxide (ITO), our analytical results can easily be applied to any LEDD materials.

I. INTRODUCTION

Recent years have seen a growing interest in the optical response of plasmonic (transparent) conducting oxides and nitrides such as aluminum- or gallium-doped zinc oxide, cadmium oxide, indium tin oxide, titanium or zirconium nitride, etc. [1–7] as alternatives to noble metals. These materials are characterized by low electron densities and high-frequency interband transitions, such that they are usually described as Drude metals at optical and telecom frequencies [1]. In comparison to noble metals, the real part of their permittivities has a milder negative value and the electron density (hence, the permittivity) is highly tunable (e.g., via doping [1,8] or post-treatment, etc. [9–11]), so that together with their CMOS compatibility, they enable flexibility of design and implementation [1,7]. In what follows, we refer to this class of materials as low-electron-density Drude (LEDD) materials.

Particular attention has been paid to the unique epsilon-near-zero (ENZ) point that these materials have in the near-infrared spectral range [2,5,12–14]. While most earlier interest in ENZ materials has been associated with

their linear response (e.g., in the context of supercoupling [15,16] or shaping the radiation pattern of a source [17,18]), the claim that the nonlinear optical response is inversely proportional to the (unperturbed vanishing) permittivity has attracted a range of experimental studies of the (ultrafast) dynamics of the permittivity near the ENZ point (see, e.g., Refs. [2,4,12,13,19–21]). In parallel, the importance of the deviation of the band structure from a simple parabolic dependence has been realized [3,4,9,22]. From the theoretical point of view, most attention has been given to modeling the dependence of the LEDD permittivity on the electron temperature using thermal models [4, 19,23,24], while the temperature dynamics itself has been described using the relaxation-time-approximation- (RTA) based two-temperature model (TTM) or its extension [3, 4,12,19,20,23]. However, frequently the TTM parameters have been computed from equations suitable for parabolic bands and high-electron-density metals. In that regard, the accuracy of the temperature modeling in LEDD materials has not yet been verified using an underlying electronic model.

Our goal in the current work is to compute consistently the nonequilibrium electron dynamics in LEDD materials. We employ the techniques previously used in the context of noble metals to go beyond the state-of-the-art modeling of LEDD materials and provide a model for their electronic and thermal dynamical response. We focus on indium tin

---

*subhajit@post.bgu.ac.il
†These two authors have contributed equally.
‡iengwai@post.bgu.ac.il
§sivanyon@bgu.ac.il

oxide (ITO) as a prototypical example. In particular, in Sec. II, we derive the various terms in the simplest model available for electron nonequilibrium, namely, the Boltzmann equation (BE), without resorting to the RTA; we complement the BE with a self-consistent treatment of the phonon system. We find that due to the low electron density and hence the weaker screening, the electron-electron (*e*-*e*) collisions are 10 times faster than in the higher-electron-density noble metals. We also find that for the same reason, the requirement of momentum conservation in electron-phonon (*e*-ph) interactions significantly slows down the collision rate; however, due to the opposing effect of the higher Debye energy, the *e*-ph collision rate is actually similar to that in noble metals. In Sec. III A, we describe the resulting ultrafast dynamics of the electron distribution and correlate them with the relative importance of the various underlying collision mechanisms. In Sec. III B, we derive analytical expressions for the TTM parameters and find that the dependence of both the heat capacity and the chemical potential on the electron temperature is much stronger than assumed so far and that their values are much lower compared to those for noble metals. We then extract the temperature dynamics from the BE and show an excellent match with the TTM. Our main results are that the electron heating is much stronger and its decay is much faster in ITO than realized before as well as compared to noble metals due to the lower electron heat capacity. In Sec. IV, we conclude with further comparison to more advanced theoretical approaches and with a discussion of future steps.

II. MODEL FOR THE ELECTRON DISTRIBUTION

We determine the electron distribution in LEDD materials by solving the quantumlike BE. This model is in wide use for Drude metals [25–33]. We focus on indium

tin oxide (ITO) because it has all the unique features of a LEDD material, namely, a low electron density and a nonparabolic conduction band and because it emerges as a promising CMOS-compatible nonlinear optical material. We also neglect interband (*d* to *sp*) transitions that occur in ITO only for photons having energies larger than 3–3.5 eV [34]; these transitions, however, set the value of the background permittivity, ε_b.

The energy-momentum ($\mathcal{E}$-k) relation of ITO can be expressed by the Kane quasilinear dispersion [35] to account for the nonparabolicity [23,36], namely,

$$\frac{\hbar^2 k^2}{2m_e^*} = \mathcal{E}(1 + C\mathcal{E}), \qquad (1)$$

where $m_e^* = 0.3964 m_e$ is the electron effective mass at the conduction-band minimum and $C = 0.4191 \text{ eV}^{-1}$ [9] is the first-order nonparabolicity factor. The electron density of states (eDOS) becomes

$$\rho_e(\mathcal{E}) = \frac{1 + 2C\mathcal{E}}{2\pi^2} \left(\frac{2m_e^*}{\hbar^2} \right)^{3/2} \sqrt{\mathcal{E}(1 + C\mathcal{E})}. \qquad (2)$$

Compared with the case in which $C = 0$ (no nonparabolicity), the density of states when $C \neq 0$ is a superlinear function (instead of a radical function) of the electron energy and is larger by a factor of $\sqrt{1 + C\mathcal{E}}(1 + 2C\mathcal{E})$ [see Fig. 1(a)]. The $\mathcal{E}$-k relation (1) allows us to represent the electron states in terms of energy $\mathcal{E}$ rather than momentum.

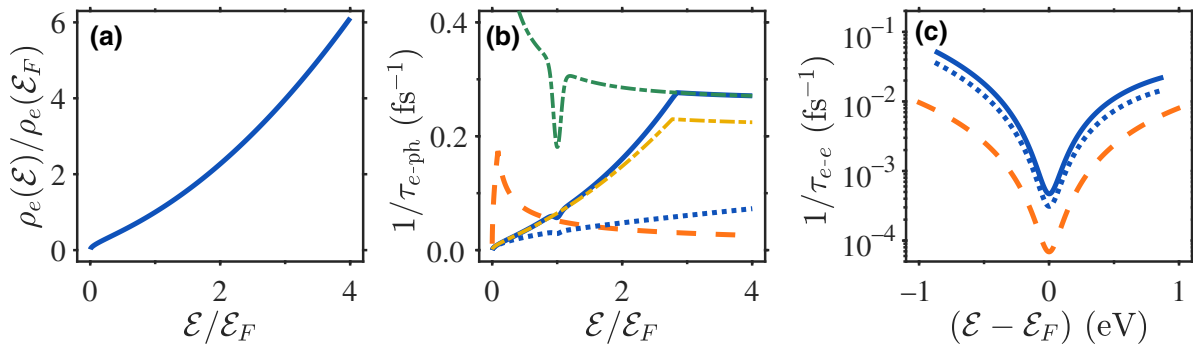The Boltzmann equation representing the electron dynamics is

FIG. 1. (a) The normalized eDOS $\rho_e(\mathcal{E})/\rho_e(\mathcal{E}_F)$ as a function of $\mathcal{E}/\mathcal{E}_F$. (b) The *e*-ph collision rate $1/\tau_{e\text{-ph}}$ (12) for the case of $C \neq 0$ (i.e., the nonparabolic band) with (blue solid line) and without (green dash-dotted line) accounting for momentum conservation. The blue dotted line represents the case accounting for momentum conservation but not for nonparabolicity (i.e., $C = 0$). The dark yellow dash-dotted line represents the approximation of the *e*-ph collision rate (13). (c) The thermalization rate associated with the *e*-*e* interaction with (blue solid line, $C \neq 0$) and without nonparabolicity (blue dotted line, $C = 0$) as a function of ($\mathcal{E} - \mathcal{E}_F$). The orange dashed lines in (b) and (c) represent the *e*-ph and *e*-*e* collision rates of Au, respectively. The collision rates in (b) and (c) are calculated at $T_e = 500$ K and $T_{\text{ph}} = 300$ K.

$$\frac{\partial f}{\partial t} = \left(\frac{\partial f}{\partial t}\right)_{\text{exc}} + \left(\frac{\partial f}{\partial t}\right)_{e\text{-ph collision}} + \left(\frac{\partial f}{\partial t}\right)_{e\text{-}e\text{ collision}}$$
$$+ \left(\frac{\partial f}{\partial t}\right)_{e\text{-imp collision}}, \tag{3}$$

where $f(\mathcal{E})$ is the electron distribution function at an energy $\mathcal{E}$, representing the population probability of electrons in a system characterized by a continuum of states within the conduction band; this description has been shown to be suitable for particles of Drude metals of sizes as small as a few nanometers [37].

The first term on the right-hand side (rhs) of Eq. (3) describes the excitation of conduction electrons due to photon absorption: for its explicit form, see Sec. II A. The second term on the rhs of Eq. (3) describes the population relaxation due to collisions between electrons and phonons: for its explicit form, see Sec. II B. The third term on the rhs of Eq. (3) (for its explicit form, see Sec. II C) implicitly represents the thermalization induced by *e-e* collisions, i.e., the convergence of the *non*thermal population into the *thermalized* Fermi-Dirac distribution, given by

$$f^T(\mathcal{E}; T_e) = \left(1 + e^{(\mathcal{E}-\mu)/k_B T_e}\right)^{-1}, \tag{4}$$

where $\mu(T_e)$ is the chemical potential, k_B is the Boltzmann constant, and T_e is the electron temperature. Note that collisions of conduction electrons with impurities may also be included, but while those contribute to the permittivity, they have no effect on the electron distribution itself [on the level of the BE (3); for details, see Appendix B [26]].

Our model does not account for electron acceleration due to the force exerted on them by the electric field (which involves a classical description; see discussion in Refs. [38,39]), nor for drift due to its gradients or due to temperature gradients; these effects may only be important for nanostructures with complex geometries. Similar simplifications have been adopted in most previous studies of electron nonequilibrium in Drude metals (see, e.g., Refs. [33,39,40]).

Below, we set the electron density in ITO to be $n_e \sim 1.5 \times 10^{27}$ m^{-3}, such that it is characterized by a relatively low Fermi energy of $\mathcal{E}_F = 0.88$ eV (compared to noble metals) and a total size of $\mathcal{E}_{\max} = 4$ eV [41,42]. However, note that due to the nonstochiometric nature of

ITO (i.e., the dependence on its preparation conditions [9,43]), the electron density in ITO can vary from 10^{27} m^{-3} to 10^{28} m^{-3} (see Ref. [42] and references therein). Similar and even lower values are typical of other LEDD materials [1].

Similarly, the values of other parameters indicated below, such as the deformation potential, the sound velocity, Debye temperature, etc., or even the impurity density or grain size, may also vary significantly from sample to sample. Yet, the analysis presented below remains generic to all ITO and other LEDD materials.

A. The quantum mechanical excitation term

The absorption of the incident light at frequency ω leads to the excitation of electrons with initial energy $\mathcal{E}_{\text{initial}} = \mathcal{E}$ to states with final energy $\mathcal{E}_{\text{final}} = \mathcal{E} + \hbar\omega$. Here, we employ the expression proposed in Refs. [32,39] to link this process to the local electric field. Specifically, the excitation term can be written as [29,32,39]

$$\left(\frac{\partial f(\mathcal{E},t)}{\partial t}\right)_{\text{exc}} = B(t)\Big[D_J(\mathcal{E}-\hbar\omega,\mathcal{E})\rho_e(\mathcal{E}-\hbar\omega)$$
$$\times f(\mathcal{E}-\hbar\omega,t)(1-f(\mathcal{E},t))$$
$$- D_J(\mathcal{E},\mathcal{E}+\hbar\omega)\rho_e(\mathcal{E}+\hbar\omega)$$
$$\times f(\mathcal{E},t)(1-f(\mathcal{E}+\hbar\omega,t))\Big]. \tag{5}$$

Here, $D_J(\mathcal{E}_{\text{initial}}, \mathcal{E}_{\text{final}})$ is the squared magnitude of the transition matrix element for the electronic process $\mathcal{E}_{\text{initial}} \to \mathcal{E}_{\text{final}}$ (be it Landau damping, surface- or phonon-assisted absorption, etc. [33,44,45]); $B(t)$ is a time-dependent coefficient ensuring energy conservation that is proportional to the local energy density or $|\mathbf{E}(t)|^2$ ($\mathbf{E}(t)$ being the *local* electric field vector in the ITO sample) [46]; in particular, the increase of the energy of the electron system is equal to the energy of the absorbed pulse (via Poynting's theorem),

$$P_{\text{abs}}(t) \equiv \int \mathcal{E}\rho_e(\mathcal{E})\left(\frac{\partial f(\mathcal{E},t)}{\partial t}\right)_{\text{exc}} d\mathcal{E} = \frac{\omega}{2}\varepsilon_0\varepsilon''|\mathbf{E}(t)|^2, \tag{6}$$

so that

$$B(t) = \frac{\varepsilon_0\varepsilon''|\mathbf{E}(t)|^2}{2\hbar \int D_J(\mathcal{E}-\hbar\omega,\mathcal{E})\rho_e(\mathcal{E})\rho_e(\mathcal{E}-\hbar\omega)f(\mathcal{E}-\hbar\omega,t)(1-f(\mathcal{E},t))d\mathcal{E}}, \tag{7}$$

where ε'' is the (static) imaginary part of the ITO permittivity.

B. The *e*-ph collision term

The collision term due to *e*-ph interaction via the deformation potential scattering is given by [47]

$$
\left(\frac{df_{\mathbf{k}}}{dt}\right)_{e\text{-ph}} = \sum_{\mathbf{q}} \frac{\pi D^2 q^2}{\rho V \omega_{\text{ph}}^{\mathbf{q}}} \left\{ \left[(n_{\text{ph}}^{\mathbf{q}} + 1)(1 - f_{\mathbf{k}})f_{\mathbf{k+q}} - n_{\text{ph}}^{\mathbf{q}}(1 - f_{\mathbf{k+q}})f_{\mathbf{k}} \right] \delta(\mathcal{E}_{\mathbf{k+q}} - \mathcal{E}_{\mathbf{k}} - \hbar\omega_{\text{ph}}^{\mathbf{q}}) \right.
$$
$$
\left. - \left[(n_{\text{ph}}^{\mathbf{q}} + 1)(1 - f_{\mathbf{k-q}})f_{\mathbf{k}} - n_{\text{ph}}^{\mathbf{q}}(1 - f_{\mathbf{k}})f_{\mathbf{k-q}} \right] \delta(\mathcal{E}_{\mathbf{k-q}} - \mathcal{E}_{\mathbf{k}} + \hbar\omega_{\text{ph}}^{\mathbf{q}}) \right\}, \tag{8}
$$

where $\mathbf{k}$ is the electron momentum, $\mathbf{q}$ is the phonon momentum, $\hbar\omega_{\text{ph}}^{\mathbf{q}}$ is the phonon energy, $\rho = 7120$ kg/m^3 is the material density [48], $D = 17.2$ eV is the deformation potential [49], and $n_{\text{ph}}^{\mathbf{q}}$ is the phonon distribution function.

For simplicity, we consider only acoustic phonons, since they have been found to be responsible for the dominant scattering mechanism compared to optical phonons [50]. We also assume that the acoustic phonons propagate at the sound velocity such that they have a linear dispersion relation, i.e., $\mathcal{E}_{\text{ph}}^{\mathbf{q}} = \hbar\omega_{\text{ph}}^{\mathbf{q}} = \hbar v_{\text{ph}} q$, where $v_{\text{ph}} = 6400$ m/s [48]. Beyond the Debye energy, $\mathcal{E}_D = k_B T_D \approx 0.06$ eV [48], the density of the phonon states vanishes. Furthermore, we assume that the phonon system is in equilibrium, so that the average phonon number satisfies the Bose-Einstein statistics and can be characterized by the phonon (lattice) temperature T_{ph}, i.e.,

$n_{\text{ph}}^{\mathbf{q}}(T_{\text{ph}}) = n_B(\mathcal{E}_{\text{ph}}^{\mathbf{q}}, T_{\text{ph}}) = \left(e^{\hbar\omega_{\text{ph}}^{\mathbf{q}}/k_B T_{\text{ph}}} - 1 \right)^{-1}$. The two terms associated with $(n_{\text{ph}}^{\mathbf{q}} + 1)$ correspond to the phonon emission, whereas the two terms associated with $n_{\text{ph}}^{\mathbf{q}}$ correspond to the phonon absorption. The delta functions in Eq. (8) ensure energy conservation in the various *e*-ph scattering processes.

To obtain the collision term as a function of the electron energy $(\partial f(\mathcal{E})/\partial t)_{e\text{-ph}}$, we perform the spherical average over the solid angle for $(df_{\mathbf{k}}/dt)_{e\text{-ph}}$ in Eq. (8), namely, $(\partial f(\mathcal{E})/\partial t)_{e\text{-ph}} = 1/4\pi \int (\partial f_{\mathbf{k}}/\partial t)_{e\text{-ph}} \, d\cos\theta_{\mathbf{k}} d\phi_{\mathbf{k}}$, where $\theta_{\mathbf{k}}$ and $\phi_{\mathbf{k}}$ are, respectively, the polar and azimuthal angles of $\mathbf{k}$ with respect to $\mathbf{q}$. In particular, we account for the phonon dispersion in the polar integral to ensure momentum conservation,

$$
\int_{-1}^{1} d\cos\theta_{\mathbf{k}} \, \delta(\mathcal{E}_{\mathbf{k}\pm\mathbf{q}} - \mathcal{E}_{\mathbf{k}} \mp \hbar\omega_{\text{ph}}^{\mathbf{q}}) = \begin{cases} \dfrac{m_e^*}{\hbar^2 k q}, & \text{if } \left| \dfrac{m_e^* v_{\text{ph}}}{\hbar k} \mp \dfrac{q}{2k} \right| \leq 1, \\ 0, & \text{otherwise.} \end{cases} \tag{9}
$$

Since $m_e^* v_{\text{ph}} \ll \hbar q_D = \hbar\mathcal{E}_D/v_{\text{ph}}$, the condition for the polar integral being nonzero in Eq. (9) can be simplified to $q \lesssim 2k$. After some algebra, we arrive at

$$
\left(\frac{\partial f(\mathcal{E})}{\partial t}\right)_{e\text{-ph}} = \frac{D^2}{4\pi\rho(\hbar v_{\text{ph}})^4} \sqrt{\frac{m_e^*}{2\mathcal{E}(1 + C\mathcal{E})}} \int_0^{\mathcal{E}_{\text{ph}}^{\text{max}}(\mathcal{E})} (\mathcal{E}_{\text{ph}})^2 d\mathcal{E}_{\text{ph}} \Big[(n_B(\mathcal{E}_{\text{ph}}, T_{\text{ph}}) + 1)
$$
$$
\times \Big((1 - f(\mathcal{E}))f(\mathcal{E} + \mathcal{E}_{\text{ph}})(1 + 2C(\mathcal{E} + \mathcal{E}_{\text{ph}})) - (1 - f(\mathcal{E} - \mathcal{E}_{\text{ph}}))f(\mathcal{E})(1 + 2C(\mathcal{E} - \mathcal{E}_{\text{ph}})) \Big)
$$
$$
+ n_B(\mathcal{E}_{\text{ph}}, T_{\text{ph}}) \Big((1 - f(\mathcal{E}))f(\mathcal{E} - \mathcal{E}_{\text{ph}})(1 + 2C(\mathcal{E} - \mathcal{E}_{\text{ph}})) - (1 - f(\mathcal{E} + \mathcal{E}_{\text{ph}})f(\mathcal{E})(1 + 2C(\mathcal{E} + \mathcal{E}_{\text{ph}})) \Big) \Big], \tag{10}
$$

where

$$
\mathcal{E}_{\text{ph}}^{\text{max}}(\mathcal{E}) = \min(\mathcal{E}_D, 2\hbar v_{\text{ph}} k(\mathcal{E})) = \begin{cases} 2\hbar v_{\text{ph}} k(\mathcal{E}), & \text{for } k(\mathcal{E}) < q_D/2, \\ \mathcal{E}_D \equiv \hbar v_{\text{ph}} q_D, & \text{for } k(\mathcal{E}) \geq q_D/2, \end{cases} \tag{11}
$$

is the maximal energy of a phonon that can be absorbed or emitted by an electron with energy $\mathcal{E}$ [51,52], $\hbar q_D = \mathcal{E}_D/v_{\text{ph}}$ is the Debye momentum, and $k(\mathcal{E})$ is the momentum of an electron with energy $\mathcal{E}$, obtained from the dispersion relation given in Eq. (1).

By taking the functional derivative of Eq. (10) with respect to $f(\mathcal{E})$ [53], we obtain the collision rate associated with the e-ph interaction, $1/\tau_{e\text{-ph}}(\mathcal{E}) = \delta\,(\partial f/\partial t)_{e\text{-ph}}\,/\delta f(\mathcal{E})$,

$$\frac{1}{\tau_{e\text{-ph}}(\mathcal{E})} = \frac{D^2}{4\pi\rho(\hbar v_{\text{ph}})^4}\sqrt{\frac{m_e^*}{2\mathcal{E}(1+C\mathcal{E})}}\int_0^{\mathcal{E}_{\text{ph}}^{\max}(\mathcal{E})}(\mathcal{E}_{\text{ph}})^2 d\mathcal{E}_{\text{ph}}\Big[(n_B(\mathcal{E}_{\text{ph}},T_{\text{ph}})+f(\mathcal{E}+\mathcal{E}_{\text{ph}}))(1+2C(\mathcal{E}+\mathcal{E}_{\text{ph}}))$$

$$+\,(n_B(\mathcal{E}_{\text{ph}},T_{\text{ph}})+1-f(\mathcal{E}-\mathcal{E}_{\text{ph}}))(1+2C(\mathcal{E}-\mathcal{E}_{\text{ph}}))\Big]. \tag{12}$$

The e-ph collision rate (12) is plotted in Fig. 1(b). It grows monotonically up to $k(\mathcal{E}) = q_D/2$ ($\mathcal{E} \sim 2.8\ \mathcal{E}_F$), beyond which point its energy dependence becomes much weaker.

To gain more insight into the dependence of $\tau_{e\text{-ph}}^{-1}$ on material parameters, we simplify Eq. (12) by expanding its integrand in a power series in $\mathcal{E}_{\text{ph}}$ since the phonon energy is small relative to the electron energy. After integration of the leading-order term of the integrand ($k_B T_{\text{ph}}\mathcal{E}_{\text{ph}}$) one obtains

$$\frac{1}{\tau_{e\text{-ph}}(\mathcal{E})} \approx \frac{D^2 k_B T_{\text{ph}}}{4\pi\rho(\hbar v_{\text{ph}})^2}\frac{m_e^*}{\hbar k(\mathcal{E})}(1+2C\mathcal{E})$$

$$\times \begin{cases} 4k^2(\mathcal{E}), & \text{for } k(\mathcal{E}) < q_D/2, \\ q_D^2, & \text{for } k(\mathcal{E}) \geq q_D/2, \end{cases} \tag{13}$$

showing decent agreement with the exact expression given in Eq. (12) [see Fig. 1(b)]. The mismatch between Eqs. (12) and (13), including the diplike feature near $\mathcal{E}_F$, can be resolved by incorporating higher-order terms. Equation (13) shows that $\tau_{e\text{-ph}}^{-1}$ is proportional to the phonon temperature as in noble metals [54] and that nonparabolicity increases $\tau_{e\text{-ph}}^{-1}$ by a factor of $k(\mathcal{E}_F)(1+2C\mathcal{E}_F) \sim \sqrt{1+C\mathcal{E}_F}(1+2C\mathcal{E}_F) \sim 2$, similar to the eDOS, as shown in Fig. 1(b).

As a comparison, we also plot the e-ph collision rate as calculated without accounting for momentum conservation. This shows that the e-ph collision rate can be strongly overestimated if momentum conservation is neglected. Indeed, due to the low electron density, the Fermi momentum ($k_F \approx 3.54$ nm^{-1}) is much smaller than the Debye momentum of ITO ($q_D \approx 14.3$ nm^{-1}), so that a substantial number of the phonons are prohibited from interacting with the electrons due to conservation of momentum. This can be further understood using a phase-space argument, as detailed in Appendix A 1. In particular, ignoring momentum conservation causes an approximately fivefold overestimate of the e-ph collision rate around the Fermi energy [see Fig. 1(b)]. Consequently, this causes a 30-fold overestimate of the energy-transfer rate between the electrons and phonons (see Sec. III B). This behavior contrasts with the situation in noble metals, for which the Debye momentum (e.g., $q_D \approx 6.85$ nm^{-1} and $q_D \approx 8.14$ nm^{-1} for Au and Ag, respectively) is smaller than their Fermi momentum ($k_F \approx 11.57$ nm^{-1} and $k_F \approx 12$ nm^{-1} for Au and Ag, respectively). For that reason, in noble metals almost all electrons can interact with all phonons, such that neglecting momentum conservation is justified. Therefore, somewhat peculiarly, the contradictory effects of the higher Debye energy in ITO [which make $\tau_{e\text{-ph}}^{-1}$ 4 times larger; see Eq. (13)] on the one hand, and the limitations on the allowed e-ph scattering events imposed by the momentum conservation (which make it approximately 5 times smaller) on the other hand, make the overall magnitude of the e-ph collision rate in ITO comparable to that in noble metals. The orange line corresponding to Au in Fig. 1(b) explicitly shows that near $\mathcal{E}_F$, the e-ph collision rates of ITO and Au are comparable.

C. The e-e collision term

The e-e interaction is responsible for the thermalization of the conduction electrons. The corresponding collision term is derived from the screened Coulomb interaction U, the potential of which in momentum space is written as

$$U(\mathbf{q}) = \frac{e^2}{4\pi\varepsilon_0\varepsilon_b}\int d^3r\frac{e^{-q_{\text{TF}}r}}{r}e^{-i\mathbf{q}\cdot\mathbf{r}} = \frac{e^2}{\varepsilon_0\varepsilon_b}\frac{1}{q^2+q_{\text{TF}}^2}, \tag{14}$$

where $\mathbf{q}$ is the exchange of momentum between two electrons and q_{TF} is the Thomas-Fermi wave vector, which is given by [29]

$$q_{\text{TF}}^2 = -\frac{4\pi^3 e^2}{\varepsilon_0\varepsilon_b}\int d\mathcal{E}\frac{\partial f}{\partial \mathcal{E}}\rho_e(\mathcal{E}), \tag{15}$$

where $\varepsilon_b = 4$ represents the contribution of interband transitions to the permittivity [21,24]. Again, following Fermi's golden rule as employed in Ref. [47] and accounting for the nonparabolicity of the conduction band, we obtain the population distribution change rate

$$\left(\frac{\partial f(\mathcal{E})}{\partial t}\right)_{e-e} = -\frac{3}{16\hbar^2}\frac{1}{(2\pi)^3}\left(\frac{e^2}{\varepsilon_0\varepsilon_b}\right)^2\left(\frac{m_e^*}{\hbar^2 q_{\mathrm{TF}}}\right)^3\frac{\hbar}{\sqrt{2m_e^*(\mathcal{E}+C\mathcal{E}^2)}}\int d\mathcal{E}_1 d\mathcal{E}_2 d\mathcal{E}_3$$

$$\times (1+2C\mathcal{E}_1)(1+2C\mathcal{E}_2)(1+2C\mathcal{E}_3)\left[\frac{qq_{\mathrm{TF}}}{q^2+q_{\mathrm{TF}}^2}+\tan^{-1}\left(\frac{q}{q_{\mathrm{TF}}}\right)\right]_{q^{\min}}^{q^{\max}}\delta(\mathcal{E}+\mathcal{E}_1-\mathcal{E}_2-\mathcal{E}_3)$$

$$\times [(1-f(\mathcal{E}_3))(1-f(\mathcal{E}_2))f(\mathcal{E}_1)f(\mathcal{E})-(1-f(\mathcal{E}))(1-f(\mathcal{E}_1))f(\mathcal{E}_2)f(\mathcal{E}_3)], \tag{16}$$

where $q^{\min} = \max(|k-k_2|,|k_1-k_3|)$ and $q^{\max} = \min(k+k_2,k_1+k_3)$. By taking the functional derivative of Eq. (16) with respect to $f(\mathcal{E})$, we obtain the collision rate associated with the *e-e* interaction,

$$\frac{1}{\tau_{e-e}(\mathcal{E})} = \frac{3}{16\hbar^2}\frac{1}{(2\pi)^3}\left(\frac{e^2}{\varepsilon_0\varepsilon_b}\right)^2\left(\frac{m_e^*}{\hbar^2 q_{\mathrm{TF}}}\right)^3\frac{\hbar}{\sqrt{2m_e^*(\mathcal{E}+C\mathcal{E}^2)}}\int d\mathcal{E}_1 d\mathcal{E}_2 d\mathcal{E}_3$$

$$\times (1+2C\mathcal{E}_1)(1+2C\mathcal{E}_2)(1+2C\mathcal{E}_3)\left[\frac{qq_{\mathrm{TF}}}{q^2+q_{\mathrm{TF}}^2}+\tan^{-1}\left(\frac{q}{q_{\mathrm{TF}}}\right)\right]_{q^{\min}}^{q^{\max}}\delta(\mathcal{E}+\mathcal{E}_1-\mathcal{E}_2-\mathcal{E}_3)$$

$$\times [(1-f(\mathcal{E}_3))(1-f(\mathcal{E}_2))f(\mathcal{E}_1)+(1-f(\mathcal{E}_1))f(\mathcal{E}_2)f(\mathcal{E}_3)]. \tag{17}$$

To gain more insight into the nonparabolicity correction to the *e-e* collision rate, we substitute the electron distribution in the integrand of Eq. (17) by the Fermi-Dirac distribution function characterized by an electron temperature T_e; after some algebra, we find

$$\frac{1}{\tau_{\text{e-e}}(\mathcal{E})} \approx K\left\{[(\pi k_B T_e)^2+(\mathcal{E}-\mu(T_e))^2]+\frac{4}{3}\frac{C(\mathcal{E}-\mu(T_e))}{(1+2C\mu(T_e))^3}(\pi k_B T_e)^2+\cdots\right\}, \tag{18}$$

where the prefactor K is given by

$$K = \frac{3}{32\hbar}\frac{1}{(2\pi)^3}\left(\frac{e^2}{\varepsilon_0\varepsilon_b}\right)^2\left(\frac{m_e^*}{\hbar^2 q_{\mathrm{TF}}}\right)^3\frac{1}{k_\mu}\left[\frac{2k_\mu q_{\mathrm{TF}}}{4k_\mu^2+q_{\mathrm{TF}}^2}+\tan^{-1}\left(\frac{2k_\mu}{q_{\mathrm{TF}}}\right)\right](1+2C\mu(T_e))^3, \tag{19}$$

in which $\mu(T_e)$ and $k_\mu = \sqrt{2m_e^*\mu(T_e)(1+C\mu(T_e))/\hbar^2}$ are the electron-temperature-dependent chemical potential and the corresponding momentum, respectively. This expression provides a generalization of Fermi liquid theory [53] to Drude materials with nonparabolic bands. Compared with the case of $C=0$, the nonparabolicity overall causes an increase of the eDOS such that the *e-e* thermalization rate increases by a factor of $(1+2C\mu(T_e))^{3/2}(1+C\mu(T_e))^{-5/4}$ [55] (approximately 1.5 for ITO at $T_e = 500$ K) and adds a small correction term that is linear with $\mathcal{E}-\mu(T_e)$ [56] [see Fig. 1(c)]. Equation (19) also shows the effect of the low electron density (and hence the smaller Fermi energy) in ITO—it not only results in a narrower energy dependence of $\tau_{\text{e-e}}^{-1}(\mathcal{E})$ but it also results in a smaller Fermi momentum and, more importantly, in weaker screening and thus a smaller Thomas-Fermi wave vector [57]. This causes the *e-e* collision rate in ITO to be approximately 10 times faster than that in Au; for an explicit comparison at $\mathcal{E} = \mu(500$ K$) + 1$ eV, see the orange dashed line in Fig. 1(c).

III. RESULTS

In the following example, we solve the BE (3) in order to obtain the electronic (i.e., solid-state physics) response of bulk ITO systems subject to (modestly high level) pulsed illumination $I_{\mathrm{inc}} = I_0 e^{-4\ln(2)(t/\tau_p)^2}$, a wavelength of 1300 nm, a duration of $\tau_p = 220$ fs, and a peak intensity of $I_0 = 2.5$ GW/cm^2. However, as for the uncertainty on the various material parameters, the following results also remain generic for other parameter values.

A. Electron dynamics

Figure 2 plots the electron distributions and the different terms corresponding to the BE in Eq. (3) at three different time slices, $t = -\tau_p/2 = -110$ fs, $t = 0$ fs, and $t = 110$ fs, corresponding to the full width at half maximum (FWHM) before the peak, at the peak, and after the peak of the pulse.

Figure 2(a) shows the initial electron distribution $f(\mathcal{E})$ as a function of the normalized energy $\mathcal{E}/\mathcal{E}_F$. The deviation from thermal equilibrium is clearly visible via the characteristic shoulders above the Fermi energy, corresponding
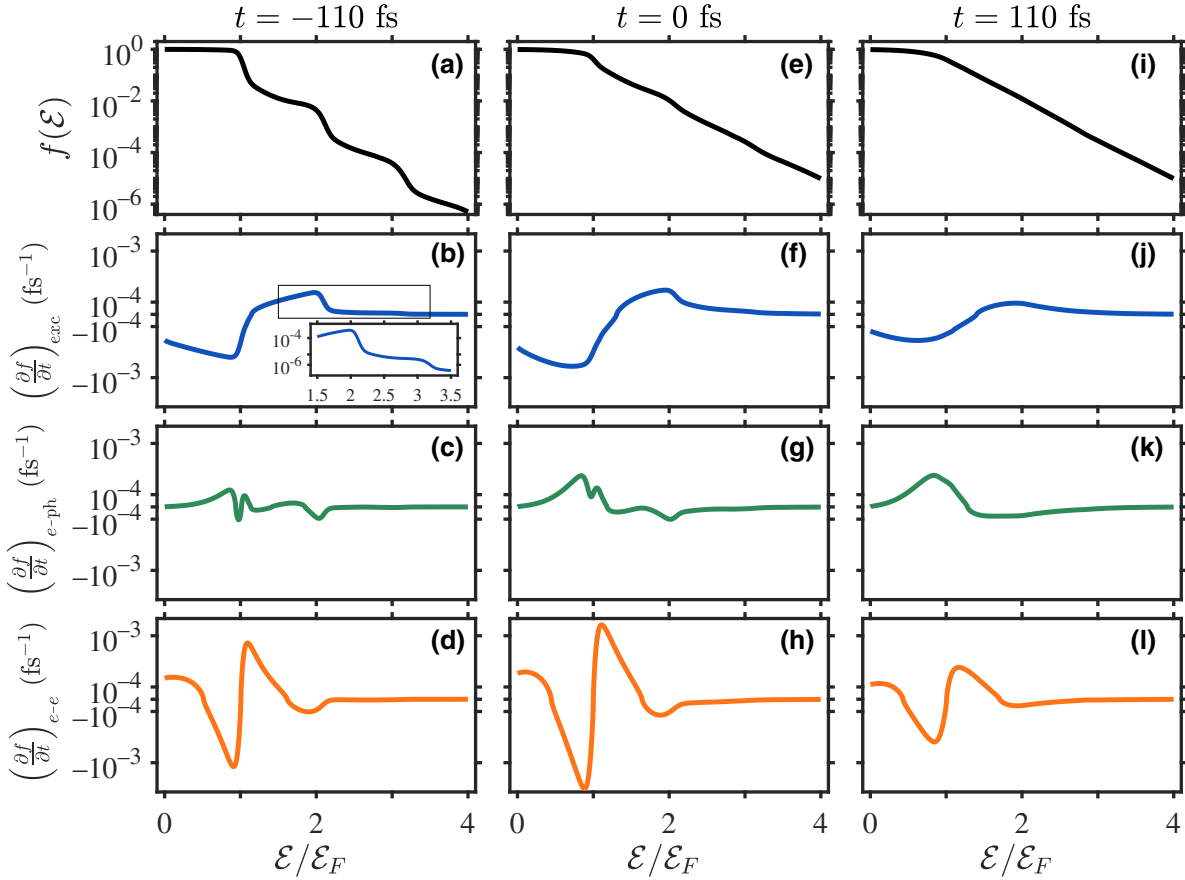
FIG. 2. (a),(e),(i) The electron distribution (black lines), (b),(f), (j) the photoexcitation (blue), (c),(g), (k) the *e*-ph interaction (green), and (d),(h),(l) the *e-e* interaction (orange) terms following the illumination of ITO by a short pulse. The left column shows the various terms at the FWHM *before* the peak of the pulse ($t = -\tau_p/2 = -110$ fs), the middle column *at the center* of the pulse ($t = 0$ fs), and the right column at the FWHM *after* the peak of the pulse ($t = +110$ fs) as a function of $\mathcal{E}/\mathcal{E}_F$ and the pulse peak intensity $I_0 = 2.5$ GW/cm^2. The inset in (b) is an enlargement of the region between $\mathcal{E} = 1.5$ eV and $\mathcal{E} = 3.5$ eV; it shows more clearly the origin of the multiple-step structure seen in (a). All terms have the same order of magnitude because of the pulsed nature of the illumination. The *y* axis is in log scale for (a), (e), and (i) and in symmetric log scale for all other subplots.

to one, two, etc., consecutive photon-absorption events; indeed, these have been observed previously for noble metals (see, e.g., Refs. [31,38,58]). They originate from the structure of the excitation term [Fig. 2(b)]. However, these shoulders gradually smooth out due to (the weak) *e*-ph collisions and (the much stronger) *e-e* collisions [see Figs. 2(c) and 2(d), respectively]. Indeed, at later times, the distribution rapidly approaches a thermal distribution [see Figs. 2(e) and 2(i)].

The corresponding evolution of the various terms is seen in the additional subplots of Fig. 2. It is interesting to note the differences with respect to the corresponding dynamics in noble metals. Specifically, due to the low Fermi energy, there is only a single $\hbar\omega$-wide region of negative rate of change of population $(\partial f/\partial t)_{\text{exc}}$ due to photon absorption below the Fermi energy but a corresponding multiple-shoulder structure of positive rate above the Fermi energy; the various shoulders are energy dependent due to the relatively strong energy dependence of the

eDOS [see Fig. 1(a)]. Moreover, near the band minimum, photon absorption is weaker due to the vanishing eDOS. This leads to a sudden cutoff of $(\partial f/\partial t)_{\text{exc}}$ (5) near the band minimum.

The structure of the *e*-ph term corresponding to Eq. (10) is significantly different compared to its structure in noble metals [see Figs. 2(c), 2(g) and 2(k)]. The origin of this difference is the importance of momentum conservation along with the number-conserving nature of the *e*-ph interaction, both of which limit the possible scattering processes (see details in Appendix A 2). Also notable is the increase in magnitude of the *e*-ph term in time; this is related to the rise of the overall electron energy and the rapid increase in the number of low-excess-energy electrons; this effect has already been shown in Ref. [28] to lead to an acceleration in the *e*-ph rate, which is not captured by the RTA.

Finally, Figs. 2(d), 2(h) and 2(l) show the rate of change of $f(\mathcal{E})$ due to *e-e* interactions corresponding to Eq. (16).

Its shape is similar to that in noble metals (cf. Ref. [39]), except near the band minimum and for $\mathcal{E} \approx \mathcal{E}_F + \hbar\omega$. This is due to the energy- and number-conserving nature of the *e-e* interaction. Near the band minimum, the positive rate of change of population is enhanced due to the vanishing eDOS.

B. Coarse-grained dynamics: The two-temperature model (TTM)

Quite frequently, it is sufficient to consider the macroscopic dynamics of the energies of the electron and phonon subsystems, respectively. This can be achieved first by integrating over the product of the various terms in the BE (3) with the electron energy and eDOS (see, e.g., Refs. [29,39]), which provides the resulting total energy of the electron subsystem. Then, a dynamic equation for the phonon energy can be written down based on the total rate of energy transfer from the electron subsystem. In order to make the resulting equations more meaningful, it is customary to rewrite the resulting energies as the product of the respective heat capacities (C_e and C_{ph}) and the electron and phonon temperatures. While the latter is well defined, it is well known that the notion of electron temperature cannot be defined clearly in the initial stages of the dynamics [28,31,59]. In this context, it is customary to *extract* an electron temperature by calculating the electron temperature T_e for which the total energy of a Fermi-Dirac (i.e., thermal) distribution f^T (4) is the same as that of the true nonthermal distribution $f(\mathcal{E})$ (3) (see, e.g., Refs. [31,33,59]), namely,

$$\mathcal{U}_e \equiv \int \mathcal{E}\rho_e(\mathcal{E})f(\mathcal{E})d\mathcal{E} = \int \mathcal{E}\rho_e(\mathcal{E})f^T(\mathcal{E}, T_e)d\mathcal{E}. \quad (20)$$

The *extracted* electron temperature emerges as a well-defined electron temperature once the distribution thermalizes [59]. Since *e-e* interactions conserve the energy of the electron subsystem, the integrated BE takes the form

$$C_e \frac{dT_e}{dt} = P_{\mathrm{abs}} - G_{e\text{-ph}}(T_e - T_{\mathrm{ph}}), \quad (21)$$

where T_e is referred to as the *effective* electron temperature. In general, the extracted and *effective* values of T_e are not the same, since thermalization is assumed to be instantaneous in Eq. (21). The equation for the phonon temperature is given by

$$C_{\mathrm{ph}} \frac{dT_{\mathrm{ph}}}{dt} = G_{e\text{-ph}}(T_e - T_{\mathrm{ph}}), \quad (22)$$

where $G_{e\text{-ph}}$ is the *e*-ph coupling. Note that since we are interested in the ultrafast dynamics, we ignore heat transfer to the environment (assumed to be at the environment temperature), as this process occurs on a much longer

time scale. Equations (21)–(22) constitute the so-called "two-temperature model"; the advantage of such a coarse-grained model is considerable, as it is significantly simpler to solve compared with the BE and it serves as the basis for temperature-based permittivity models.

The TTM parameters are usually hard to measure directly. However, as an exception, the phonon heat capacity has been measured to be $C_{\mathrm{ph}} = 2.54 \times 10^6 \ \mathrm{J\,m^{-3}\,K^{-1}}$ [60] and similar values arise from a direct calculation. More frequently, the TTM parameters are calculated theoretically using thermal distributions at the effective electron temperature. For noble metals, relatively simple expressions for the various emerging parameters can be obtained (see, e.g., Refs. [59,61]); in particular, the electron heat capacity is proportional to T_e, and the *e*-ph coupling is approximately T_e independent. These parameters, however, are significantly more complicated in LEDD materials compared to noble metals because of the nonparabolicity and especially because of the much smaller electron density (and hence the smaller Fermi energy $\mathcal{E}_F$). In principle, the TTM parameters can be evaluated through integral expressions (see Eqs. (25) and (26) below). However, in what follows, we also provide approximate analytical expressions for these parameters; these expressions are suitable for any value of the intrinsic parameters of ITO (or other LEDD materials), which indeed vary due to the fabrication and/or doping conditions (see, e.g., Refs. [1,8,9]).

One effect of the smaller $\mathcal{E}_F$ is that the dependence of the chemical potential on the temperature is not negligible as in noble metals [62]. To see this, we employ the Sommerfeld expansion [26,63] to express the total energy of the electron subsystem $\mathcal{U}_e$ as a Taylor expansion in powers of $k_B T_e$, assuming purely thermal electron distributions. In standard textbooks (e.g. Ref. [26]), the expansion is usually kept up to the second order only. However, since the Fermi energy of ITO is much lower than that of metals and since the incoming illumination intensity is strong such that the electron temperature might become non-negligible with respect to the Fermi temperature (e.g., approximately 10 000 K in ITO), one needs to keep the expansion at least up to the fourth order, namely,

$$\mathcal{U}_e \approx \int_0^{\mu(T_e)} \mathcal{E}\rho_e(\mathcal{E})d\mathcal{E} + \frac{\pi^2}{6}(k_B T_e)^2 \left. \frac{d\left(\mathcal{E}\rho_e(\mathcal{E})\right)}{d\mathcal{E}} \right|_{\mathcal{E}=\mu(T_e)}$$
$$+ \frac{7\pi^4}{360}(k_B T_e)^4 \left. \frac{d^3\left(\mathcal{E}\rho_e(\mathcal{E})\right)}{d\mathcal{E}^3} \right|_{\mathcal{E}=\mu(T_e)}. \quad (23)$$

Then, the temperature-dependent chemical potential $\mu(T_e)$ is determined using number conservation, $\int_0^\infty \rho_e(\mathcal{E})f^T(\mathcal{E}, \mu(T_e), T_e)d\mathcal{E} = \int_0^{\mathcal{E}_F} \rho_e(\mathcal{E})d\mathcal{E}$, i.e.,
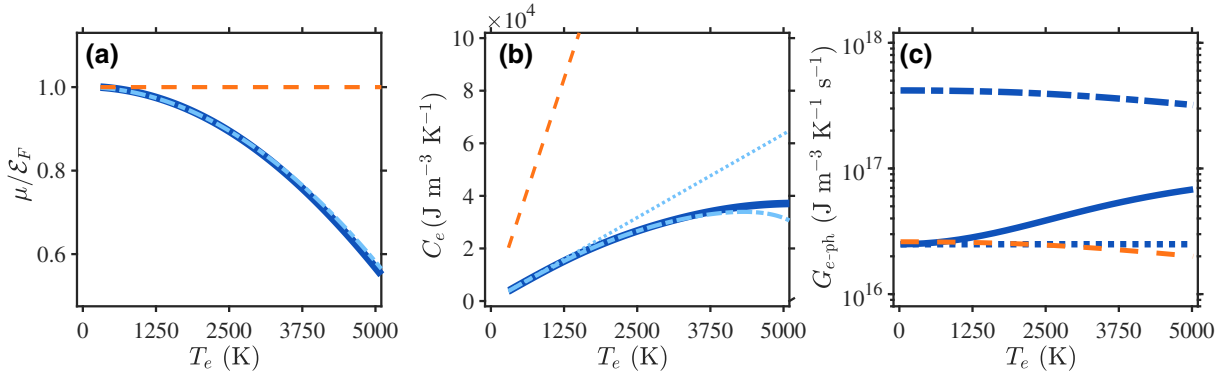
FIG. 3. (a) The chemical potential μ and (b) the electron heat capacity C_e as a function of the electron temperature T_e. The blue solid and dot-dashed lines correspond to the numerical values and analytical forms (Eqs. (24) for μ and (25) for C_e), respectively. The dotted line in (b) corresponds to the linear approximation of C_e, indicating the deviation from the linear dependence above $T_e \sim 1300$ K. (c) The e-ph coupling coefficient $G_{e\text{-ph}}$ as a function of the electron temperature [Eq. (26)] (blue solid line) and its zero-temperature limit [Eq. (28)] (blue dotted line). The blue dashed line represents the case without accounting for momentum conservation [Eq. (27)]. The orange dashed lines in (a)–(c) correspond to Au.

$$\mu(T_e) \approx \mathcal{E}_F - \frac{(\pi k_B T_e)^2}{6} \frac{1}{\rho_e(\mathcal{E}_F)} \frac{d\rho_e(\mathcal{E})}{d\mathcal{E}}\bigg|_{\mathcal{E}_F}, \tag{24}$$

where $\int_0^{\mathcal{E}_F} \rho_e(\mathcal{E})d\mathcal{E}$ is the number of electrons at zero temperature (which is indeed the same as that at 300 K). This expression is plotted in Fig. 3(a) versus the exact numerical solution. Unlike LEDD materials, the change in μ_e with T_e is quite negligible for noble metals (e.g., Au) for most practical purposes; see the orange dashed line in Fig. 3(a).

Similarly to μ, the exact integral definition of the electron heat capacity can be approximated as

$$\begin{aligned} C_e(T_e) &\equiv \frac{d\mathcal{U}_e}{dT_e} = \frac{d}{dT_e}\left[\int \mathcal{E}\rho_e(\mathcal{E})f^T(\mathcal{E}, T_e)d\mathcal{E}\right] \\ &\approx \frac{\pi^2 k_B^2}{3} T_e\left[\rho_e(\mu) + \mu\rho_e^{(1)}(\mu)\right] + \frac{7\pi^4 k_B^4}{90} T_e^3\left[3\rho_e^{(2)}(\mu) + \mu\rho_e^{(3)}(\mu)\right] \\ &\quad + \frac{d\mu}{dT_e}\left(\mu\rho_e(\mu) + \frac{(\pi k_B T_e)^2}{6}\left[2\rho_e^{(1)}(\mu) + \mu\rho_e^{(2)}(\mu)\right] + \frac{7(\pi k_B T_e)^4}{360}\left[2\rho_e^{(3)}(\mu) + \mu\rho_e^{(4)}(\mu)\right]\right), \end{aligned} \tag{25}$$

where $\rho_e^{(n)}(\mu) = d^n\rho_e(\mathcal{E})/d\mathcal{E}^n\big|_\mu$ and $\mu(T_e)$ is given by Eq. (24). As shown in Fig. 3(b), up to $T_e \sim 1300$ K, the electron heat capacity scales linearly with the electron temperature (viz. $C_e \approx \gamma_e T_e$ with $\gamma_e = \pi^2 k_B^2\left[\rho_e(\mu) + \mu\rho_e^{(1)}(\mu)\right]/3$ [64]). Note that the value of γ_e for ITO [and hence the value of C_e and its T_e dependence (12.7 J m^{-3} K^{-2})] is much smaller than for noble metals, e.g., $\gamma_e = 67.6$ J m^{-3} K^{-2} for gold (Au) [65]. This smaller value of γ_e in ITO is associated with the lower electron density; indeed, compared to noble metals, the eDOS is evaluated at the much lower chemical potential, giving rise to a smaller value for γ_e. Furthermore, the cubic dependence of C_e (emerging from the fourth-order term in the Sommerfeld expansion of the electron energy) provides decent accuracy only up to $T_e \sim 3500$ K.

In particular, in this regime of electron temperatures, C_e experiences a sublinear growth due to the decrease of μ with temperature.

Lastly, the e-ph coupling coefficient $G_{e\text{-ph}}$ can be obtained by evaluating the energy transferred from the electron to the phonon subsystem, i.e., $(\partial\mathcal{U}_e/\partial t)_{e\text{-ph}} = \int \mathcal{E}\rho_e(\mathcal{E})(\partial f/\partial t)_{e\text{-ph}}d\mathcal{E}$, where $(\partial f/\partial t)_{e\text{-ph}}$ is given by Eq. (10). As for C_e, we substitute the Fermi-Dirac distribution at the effective electron temperature for f and expand the integrand in a power series in $\mathcal{E}_{\text{ph}}$. Similar to noble metals, we find that the leading-order term is proportional to the difference between the electron and phonon temperatures, i.e., $(\partial\mathcal{U}_e/\partial t)_{e\text{-ph}} \approx -G_{e\text{-ph}}(T_e - T_{\text{ph}})$, where the e-ph coupling coefficient is given by

$$G_{e\text{-ph}}(T_e) = \frac{D^2 m_e^* k_B}{4(\pi\hbar)^3 \rho (\hbar v_{\text{ph}})^4} \int_0^\infty d\mathcal{E} \int_0^{\mathcal{E}_D} (\mathcal{E}_{\text{ph}})^2 d\mathcal{E}_{\text{ph}}$$

$$\times \left[(1 + 2C\mathcal{E})\text{sech}^2 \left(\frac{\mathcal{E} - \mu}{2k_B T_e} \right) \tanh \left(\frac{\mathcal{E} - \mu}{2k_B T_e} \right) - 4Ck_B T_e \text{sech}^2 \left(\frac{\mathcal{E} - \mu}{2k_B T_e} \right) \right]$$

$$- \frac{D^2 m_e^* k_B}{4(\pi\hbar)^3 \rho (\hbar v_{\text{ph}})^4} \left\{ \int_0^\infty d\mathcal{E} \int_0^{\mathcal{E}_{\text{ph}}^{\text{max}}} (\mathcal{E}_{\text{ph}})^2 d\mathcal{E}_{\text{ph}} \right.$$

$$\times \left[(1 + 2C\mathcal{E})\text{sech}^2 \left(\frac{\mathcal{E} - \mu}{2k_B T_e} \right) \tanh \left(\frac{\mathcal{E} - \mu}{2k_B T_e} \right) - 4Ck_B T_e \text{sech}^2 \left(\frac{\mathcal{E} - \mu}{2k_B T_e} \right) \right]$$

$$\left. - \int_0^{\mathcal{E}_{\text{min},D}} d\mathcal{E} \left[\frac{8(m_e^* v_{\text{ph}}^2)^2}{k_B T_e} \mathcal{E}^2 (1 + C\mathcal{E})(1 + 2C\mathcal{E})^3 \text{sech}^2 \left(\frac{\mathcal{E} - \mu}{2k_B T_e} \right) \right] \right\}, \tag{26}$$

and where $\mathcal{E}_{\text{ph}}^{\text{max}}$ is given by Eq. (11).

Similar to the other TTM parameters, the *e*-ph coupling coefficient $G_{e\text{-ph}}$ attains a different and more complex form compared to noble metals. Indeed, we plot the electron-temperature dependence of $G_{e\text{-ph}}$ (26) in Fig. 3(c). First, we find that the magnitude of $G_{e\text{-ph}}$ of ITO (approximately 3×10^{16} J m^{-3} K^{-1} s^{-1}) is similar to that of Au (approximately 2.5×10^{16} J m^{-3} K^{-1} s^{-1} [29,66,67]) although the Debye energy of ITO is 4 times larger than that of Au. The reason is that conservation of momentum prohibits a large portion of the phonons from interacting with the electrons, similar to the *e*-ph collision rate in Sec. II B. Second, Fig. 3(c) shows that quite different from noble metals, $G_{e\text{-ph}}$ of ITO increases with the electron temperature. This is again a direct result of the momentum-conservation constraint. In general, the momentum conservation in *e*-ph collision ensures that electrons with momentum $\hbar k$ can only absorb or emit phonons with momentum ranging from 0 to $2\hbar k$ (see details in Appendix A 1). In ITO, the momentum of many of the electrons is much smaller than the Debye momentum (due to $k_F = q_D/4$), so the maximal momentum of a phonon that can be absorbed or emitted by an electron increases with the momentum of the electron. Therefore, when the electron temperature increases, more electrons occupy higher-energy states; these higher-energy electrons can then interact with higher-energy phonons, leading to faster transfer of energy from the electrons to the phonon subsystem and, thus, to an increase in $G_{e\text{-ph}}$ [68]. In contrast, in noble metals, the momentum of electrons is much larger than the Debye momentum, so that the maximal energy of a phonon that can be absorbed or emitted by electrons is limited by the Debye momentum instead of the electron momentum, so that $G_{e\text{-ph}}$ is independent of the electron temperature [29,30,39,69,70].

To gain more insight into $G_{e\text{-ph}}$, we analyze Eq. (26) in some simple limits. First, we consider the *e*-ph coupling coefficient without accounting for momentum conservation. This corresponds to the first term (the first two lines)

in Eq. (26), and it can be simplified to be (see Eq. (A4))

$$G_{e\text{-ph}}(T_e) = \frac{D^2 m_e^{*2} k_B \mathcal{E}_D^4}{16(\pi\hbar)^3 \rho (\hbar v_{\text{ph}})^4} (1 + 2C\mu(T_e))^2$$

(without momentum conservation). (27)

This approximation is widely used in modeling of noble metals [29,30,39,69,70]; however, it is poor for ITO. Indeed, the ratio between Eqs. (26) and Eq. (27) shows that $G_{e\text{-ph}}$ is smaller than that of the case without accounting for momentum conservation by a factor of $(\mathcal{E}_D/2\hbar v_{\text{ph}} k_F)^4$ (approximately 30) [see Fig. 3(c)]. Furthermore, due to the nonparabolicity, the *e*-ph coupling coefficient (27) is larger by an overall factor of $(1 + 2C\mu)^2$ (approximately 3 for ITO) and shows an (incorrect) decrease with the electron temperature (due to the decrease of chemical potential μ with the electron temperature T_e) [see Fig. 3(c)]. For a more accurate approximation, we consider the *e*-ph coupling coefficient with momentum conservation in the zero-temperature limit. In this case, Eq. (26) becomes (see Appendix A 3)

$$G_{e\text{-ph}}(T_e \to 0 \text{ K}) = \frac{D^2 m_e^{*2} k_B k_F^4}{\pi^3 \rho \hbar^3} (1 + 2C\mathcal{E}_F)^2$$

($k_F < q_D/2$ and momentum conserved). (28)

Having determined the various parameters appearing in the TTM equations, we can solve them and plot the resulting (effective) electron as well as the phonon-temperature dynamics in Fig. 4. Figure 4(a) shows that the numerical value of the *extracted* T_e is similar to that of the *effective* T_e. This is due to the thermalization time being much shorter than the pulse duration. We further compare the temperature dynamics of ITO to those of the noble metals, e.g., Au, for the same heat source (6). Overall, the dynamics in these two systems are qualitatively similar, namely, the electron temperature grows on a time scale of
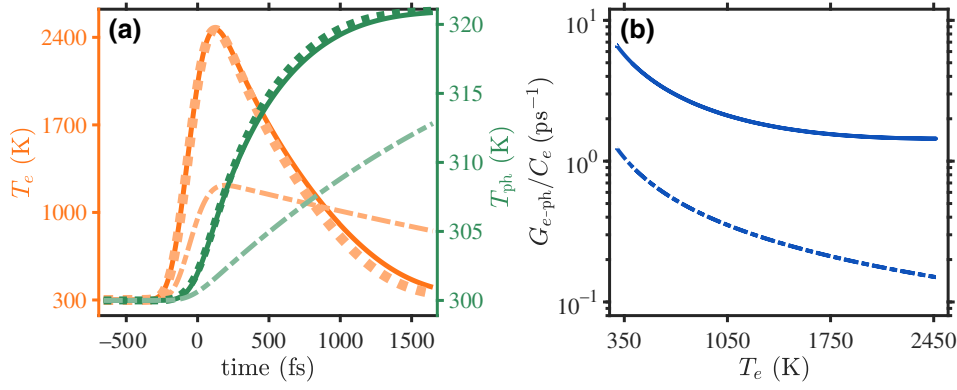
FIG. 4. (a) The electron temperatures (orange lines) and phonon temperatures (green lines) as a function of time for the pulse parameters specified in the text. The solid and dotted lines correspond to *extracted* T_e [using Eqs. (20) and (22)] and *effective* T_e [the solution of Eqs. (21)–(22)], respectively. The dot-dashed lines correspond to the temperature dynamics of Au obtained from the TTM simulation with $C_e = \gamma_e T_e$ (with $\gamma_e = 67.6 \, \mathrm{J\,m^{-3}\,K^{-2}}$ [65]) and e-ph coupling $G_{e\text{-ph}} = 2.5 \times 10^{16} \, \mathrm{J\,m^{-3}\,K^{-1}\,s^{-1}}$ [29,66]. (b) The ratio $G_{e\text{-ph}}/C_e$ for ITO (solid line) and Au (dot-dashed line).

a few hundred femtoseconds (dictated by the pulse duration) and then decays due to e-ph interactions. However, the total electron heating in ITO is much higher than in Au. The reason for that is the difference in the values of the corresponding heat capacities; indeed, at low temperatures, the electron heat capacity is linear with the electron temperature (i.e., $C_e \sim \gamma_e T_e$) and γ_e for ITO is about 5 times smaller than in Au (as already mentioned above, $\gamma_e = 67.6 \, \mathrm{J\,m^{-3}\,K^{-2}}$ in Au [65] and $\gamma_e = 12.7 \, \mathrm{J\,m^{-3}\,K^{-2}}$ obtained for ITO). As a rough estimate, one can ignore e-ph heat transfer in the initial stages of the dynamics, so that the temperature rise can be easily shown to scale as $\sqrt{\mathcal{U}_{\mathrm{abs}}/\gamma_e}$ (see, e.g., Ref. [71]). The ratio of the maximal temperature rise in ITO and Au (approximately 2100 K and approximately 900 K, respectively) is indeed given roughly by $\sqrt{67.6/12.7} \sim 2.3$.

Another notable difference is that the rate of decrease of the (effective) electron temperature (and, correspondingly, the rise time of the phonon temperature) is faster in ITO compared to Au [see Fig. 4(a)]. To leading order, these rates are determined by the ratio $G_{e\text{-ph}}(T_e - T_{\mathrm{ph}})/C_e$; since C_e is lower and T_e is higher in ITO but $G_{e\text{-ph}}$ is comparable in ITO and Au, the rates in ITO are higher [see Fig. 4(b)]. Nevertheless, since the phonon heat capacity and the heat absorption are similar in both ITO and Au, the eventual phonon temperature reached is similar in the two systems (not shown).

IV. DISCUSSION AND OUTLOOK

We see that the lower electron density along with the nonparabolicity distinguishes the electron and heat dynamics in ITO (and, more generally, LEDD materials) from those in noble metals. In particular, we identify significant differences in the e-ph interactions, a faster e-e collision rate, a much stronger dependence of the TTM parameters on the electron temperature, and a different overall heating and dynamics due to a lower electron heat capacity. The analytical expressions obtained for the TTM parameters allow an easy investigation of other LEDD materials.

We also show that the TTM matches remarkably well the dynamics of the *extracted* electron temperature as well as those of the phonon temperature. Nevertheless, the TTM has known limitations in noble metals; in particular, it assumes *a priori* that the e-e scattering is fast enough to establish a thermal distribution of electrons before significant energy is transferred to the phonons and it cannot account for the accelerating rate of e-ph collisions [28]. While this is a problematic assumption for noble metals, it has been shown in Ref. [72] that this assumption holds well in light metals such as Na, Cs, Rb, and K. In that respect, the condition of validity of the TTM in ITO does not strictly hold; yet the faster e-e collision rate makes it closer to being satisfied in comparison to noble metals.

In order to improve upon the TTM, it is customary to add a dynamical equation for the total nonthermal energy (see, e.g., Refs. [39,73–76] for noble metals or Ref. [12] for ITO); this is usually done within the RTA, requiring a somewhat ambiguous choice of an energy-averaged decay coefficients of the nonthermal energy to the (thermal) electron and phonon subsystems. Whether or not such an improvement is necessary requires a rigorous consideration of the permittivity (or, for example, the reflectivity) dynamics; this might reveal differences between the thermal and nonthermal dynamics. This complicated task is left for a future paper.

In this vein, the current work is a starting point for modeling the permittivity dynamics of ITO and other LEDD materials, as well as the observed spectral broadening and fast switching, both for pulses that are a few hundred femtoseconds long as well as shorter ones. In this

context, it would be of great interest to unravel the physical mechanism underlying the nonlinear optical response of ITO at increasingly high illumination intensities. Our formulation can provide the explanation for the high damage threshold, a key to any application, and the decrease of the reflection decay rate with the pump peak intensity observed in Ref. [77]. Our work is the starting point for the study of the nonlinear response at higher intensities and shorter pulses, enabling a list of applications such as pulse shaping and optical switching, efficient frequency conversion, terahertz emission, etc. [1,7]. Given that ITO is a CMOS-compatible material, all of these important applications are directly relevant to our findings since these applications require a thorough understanding of the electron dynamics and the associated nonlinear response. Moreover, heat management in optical communication systems is a major concern for the development of modern data centers. As such, an improved understanding of the heat dynamics in ITO systems is crucial to optical communication systems.

APPENDIX A: THE *e*-ph COLLISION TERM AND THE *e*-ph COUPLING COEFFICIENT

1. The phase-space argument for *e*-ph scattering

In the main text, we assert that the *e*-ph collision term, the corresponding energy exchange rate, and the coupling

coefficient can be dramatically overestimated in ITO if momentum conservation is not taken into consideration. However, since it is difficult to deduce how conservation of momentum is manifested in Eqs. (9)–(12), we provide below a detailed phase-space argument.

Let us consider an electron that initially has an energy $\mathcal{E}_1$ interacting with phonons having energy $\mathcal{E}_{ph,1}$ or $\mathcal{E}_{ph,2}$, as shown by the green and red diamonds, respectively, in Figs. 5(a) and 5(c). Without loss of generality, we assume that the electron initially has momentum $(0, k_1 = \sqrt{2m_e^* \mathcal{E}_1 (1 + C\mathcal{E}_1)}/\hbar, 0)$, represented by the black dot in momentum space [see Fig. 5(b)]. If the electron absorbs the phonon with energy $\mathcal{E}_{ph,1}$, the energy of the electron is changed to $\mathcal{E}_1 + \mathcal{E}_{ph,1}$ due to the conservation of energy. The possible final states can then be represented by a sphere (a circle on the $k_z = 0$ plane) the radius of which is equal to the magnitude of the momentum $\sqrt{2m_e^* (\mathcal{E} + \mathcal{E}_{ph,1})(1 + C(\mathcal{E} + \mathcal{E}_{ph,1}))}/\hbar$, represented by the green circle in Fig. 5(b). Meanwhile, the momentum of the electron is changed to $(0, k_1, 0) + \mathbf{q}_1$ due to conservation of momentum, where $\mathbf{q}_1$ is the momentum of the absorbed phonon satisfying the linear energy-momentum dispersion $q_1 = \mathcal{E}_{ph,1}/(\hbar v_{ph})$ as shown in Fig. 5(c). The possible final states satisfying momentum conservation can then be represented by a sphere (a circle on the $k_z = 0$ plane) centered at $(0, k_1, 0)$ and having a radius of q_1 [the green dashed circle in Fig. 5(b)] in momentum space. Therefore, the true possible final electron states satisfying both energy and momentum conservation can then be identified by the intersection of these two spheres in the three-dimensional (3D) momentum space (two circles on the $k_z = 0$ plane), as shown by the green dot in Fig. 5(b).

Now, if the initial electron were to interact with the phonon with energy $\mathcal{E}_{ph,2}$ and momentum $\mathbf{q}_2$, the final
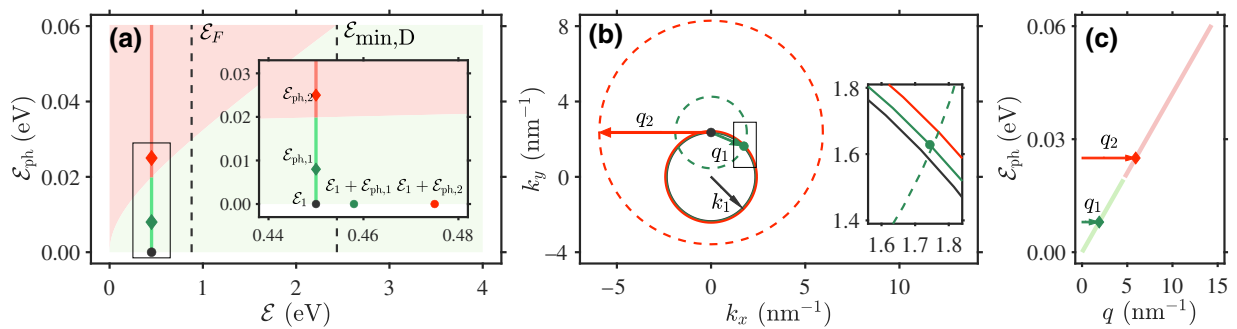

FIG. 5. (a) A plot showing the possibility of interaction between electrons with energy $\mathcal{E}$ and phonons with energy $\mathcal{E}_{ph}$: green, interacting; red, noninteracting. The inset shows that electrons with energy $\mathcal{E}_1$ can absorb a phonon with energy $\mathcal{E}_{ph,1}$ but cannot absorb a phonon with energy $\mathcal{E}_{ph,2}$. (b) The phase-space argument of the *e*-ph interaction. The black, green, and red circles, respectively, represent the states having energies $\mathcal{E}_1$, $\mathcal{E}_1 + \mathcal{E}_{ph,1}$ and $\mathcal{E}_1 + \mathcal{E}_{ph,2}$ on the $k_z = 0$ plane in the momentum space. The green (red) dashed circles represent the possible states that can be reached if an electron with energy $\mathcal{E}_1$ and momentum $(0, k_1, 0)$ (black dot) absorbs a phonon with energy $\mathcal{E}_{ph,1}$ ($\mathcal{E}_{ph,2}$). The intersection between the green solid and dashed circles represents the final electron state of the scattering process. No intersection between the red solid and dashed circles indicates that no final state can be reached. (c) The linear energy-momentum relation of the acoustic phonon. The phonon states with energy $\mathcal{E}_{ph,1}$ ($\mathcal{E}_{ph,2}$) and momentum q_1 (q_2) are represented by the green (red) diamonds.

electron would have energy $\mathcal{E}_1 + \mathcal{E}_{\text{ph},2}$ [represented by the red circle in Fig. 5(b)] and momentum $(0, k_1, 0) + \mathbf{q}_2$ [represented by the red dashed circle in Fig. 5(b)]. However, these two circles (two spheres in the 3D momentum space) do not intersect each other, indicating that no final state can be reached and thus the electrons with energy $\mathcal{E}_1$ do not interact with the phonons with energy $\mathcal{E}_{\text{ph},2}$.

Since the phonon energy is usually much smaller than the electron energy ($\mathcal{E}_D \ll \mathcal{E}_1$ in the above example), the initial and final energies ($\mathcal{E}_1$ and $\mathcal{E}_1 + \mathcal{E}_{\text{ph},1}$, respectively) of the electron are very close to each other [that is why the black, green, and red circles nearly overlap with each other in Fig. 5(b)]. However, the initial and final momentum of the electron can be very different and the magnitude of the momentum difference can range from 0 to approximately $2k_1$. Therefore, electrons with momentum k_1 (energy $\mathcal{E}_1$) interact only with phonons having momentum smaller than approximately $2k_1$ [energy smaller than $\sqrt{8m_e^* v_{\text{ph}}^2 \mathcal{E}_1(1 + C\mathcal{E}_1)}$, represented by the light green line in Figs. 5(a) and 5(c)] [78]. This happens for electrons having momentum smaller than $q_D/2$ (or energy smaller than

$\mathcal{E}_{\text{min},D} = 1/2C\left(\sqrt{1 + C\mathcal{E}_D^2/2m_e^* v_{\text{ph}}^2} - 1\right)$) [see Fig. 5(a)]. For ITO, $q_D/2 \approx 2k_F$ is much larger than the Fermi momentum ($\mathcal{E}_{\text{min},D} \approx 2.46$ eV is much larger than its Fermi energy), such that a substantial number of phonons are prohibited from interacting with electrons [see Fig. 5(a)], resulting in a much smaller e-ph coupling coefficient than that without accounting for momentum conservation in the e-ph collisions [see the comparison shown in Fig. 3(c)].

2. The function shape of the e-ph collision term in the Boltzmann equation

The conservation of momentum not only reduces the number of phonons available for e-ph collisions but also causes $(\partial f(\mathcal{E})/\partial t)_{e\text{-ph}}$ to exhibit a very different shape from the shape characteristic of noble metals (see, e.g., Refs. [30,39,59]), as shown in Figs. 2(c), 2(g), 2(k), and 6(a)–6(c). To gain a deeper understanding of this, we simplify Eq. (10) by expanding its integrand in a power series in $\mathcal{E}_{\text{ph}}$. After some algebra, we find that $(\partial f(\mathcal{E})/\partial t)_{e\text{-ph}}$ is dominated by three terms, namely,

$$\left(\frac{\partial f(\mathcal{E})}{\partial t}\right)_{e\text{-ph}} \approx \frac{D^2}{4\pi\rho(\hbar v_{\text{ph}})^4}\sqrt{\frac{m_e^*}{2\mathcal{E}(1 + C\mathcal{E})}}(1 + 2C\mathcal{E})\left[\frac{(\mathcal{E}_{\text{ph}}^{\max})^4}{4}\frac{\partial}{\partial\mathcal{E}}(f(\mathcal{E})(1 - f(\mathcal{E}))) + \frac{(\mathcal{E}_{\text{ph}}^{\max})^5}{5}\frac{\partial^2}{\partial\mathcal{E}^2}f(\mathcal{E})\right.$$
$$\left. + 96(m_e^* v_{\text{ph}}^2)^2\mathcal{E}(1 + C\mathcal{E})(1 + 2C\mathcal{E})f(\mathcal{E})(1 - f(\mathcal{E}))H(\mathcal{E})H(\mathcal{E}_{\text{min},D} - \mathcal{E})\right], \tag{A1}$$

where $\mathcal{E}_{\text{ph}}^{\max}(\mathcal{E}) = \min(\mathcal{E}_D, \sqrt{8m_e^* v_{\text{ph}}^2\mathcal{E}(1 + C\mathcal{E})})$ is the maximal energy of a phonon that can be absorbed or emitted by an electron with energy $\mathcal{E}$ [the boundary between the green and red regimes in Fig. 6(a)]. The first term is proportional to the first derivative of $f(\mathcal{E})(1 - f(\mathcal{E}))$ with respect to $\mathcal{E}$. The second term is proportional to the second derivative of $f(\mathcal{E})$ with respect to $\mathcal{E}$. The third term is proportional to $f(\mathcal{E})(1 - f(\mathcal{E}))$; it is nonzero only for $0 < \mathcal{E} < \mathcal{E}_{\text{min},D}$ (see the two Heaviside step functions) and it ensures electron-number conservation in the e-ph interaction, i.e., $\int \rho_e(\mathcal{E})(\partial f/\partial t)_{e\text{-ph}} d\mathcal{E} = 0$. For noble metals, $\mathcal{E}_{\text{min},D}$ is much smaller than Fermi energy such that $\mathcal{E}_{\text{ph}}^{\max}(\mathcal{E}) = \mathcal{E}_D$ for most of the electrons and the contribution from the third term becomes negligible. In this case, Eq. (A1) reduces to the usual differential form of the e-ph collision [30].

Figures 6(d)–6(l) show the three terms in Eq. (A1) as a function of the electron energy at three different times: before ($t = -110$ fs), at the center of ($t = 0$ fs), and after ($t = +110$ fs) the peak of the pulse. The shape of these

three terms can be explained by the (smeared) multi-stair-step structure of $f(\mathcal{E})$ [see Fig. 2(a)]. Since the third term in Eq. (A1) has the simplest form (proportional to approximately $f(\mathcal{E})(1 - f(\mathcal{E}))$) and the first term is proportional to the first derivative of $f(\mathcal{E})(1 - f(\mathcal{E}))$, we start by explaining the function shape of the third term, then the first term, and lastly the second term.

To explain the function shape of the third term, we first look at the multi-stair-step shape of $f(\mathcal{E})$ at $t = -110$ fs as shown in Fig. 2(a). The step of $f(\mathcal{E})$ near $\mathcal{E}_F$ is due to the Fermi-Dirac nature. Around this step, $f(\mathcal{E})$ changes from approximately 1 to approximately 0, while $1 - f(\mathcal{E})$ changes from approximately 0 to approximately 1. This leads to a peak in the third term of Eq. (A1) (approximately $f(\mathcal{E})(1 - f(\mathcal{E}))$) near the Fermi energy [see Fig. 6(j)]. The small step of $f(\mathcal{E})$ near $\mathcal{E}_F + \hbar\omega$ is created by the photon absorption (the nonthermal shoulder). Around this step, $f(\mathcal{E})$ changes from approximately 10^{-2} to approximately 10^{-4}, while $1 - f(\mathcal{E})$ is nearly equal to 1. This causes the third term of Eq. (A1) (approximately $f(\mathcal{E})(1 - f(\mathcal{E}))$) to have a steplike shape near $\mathcal{E}_F + \hbar\omega$ (instead of a peak) [see
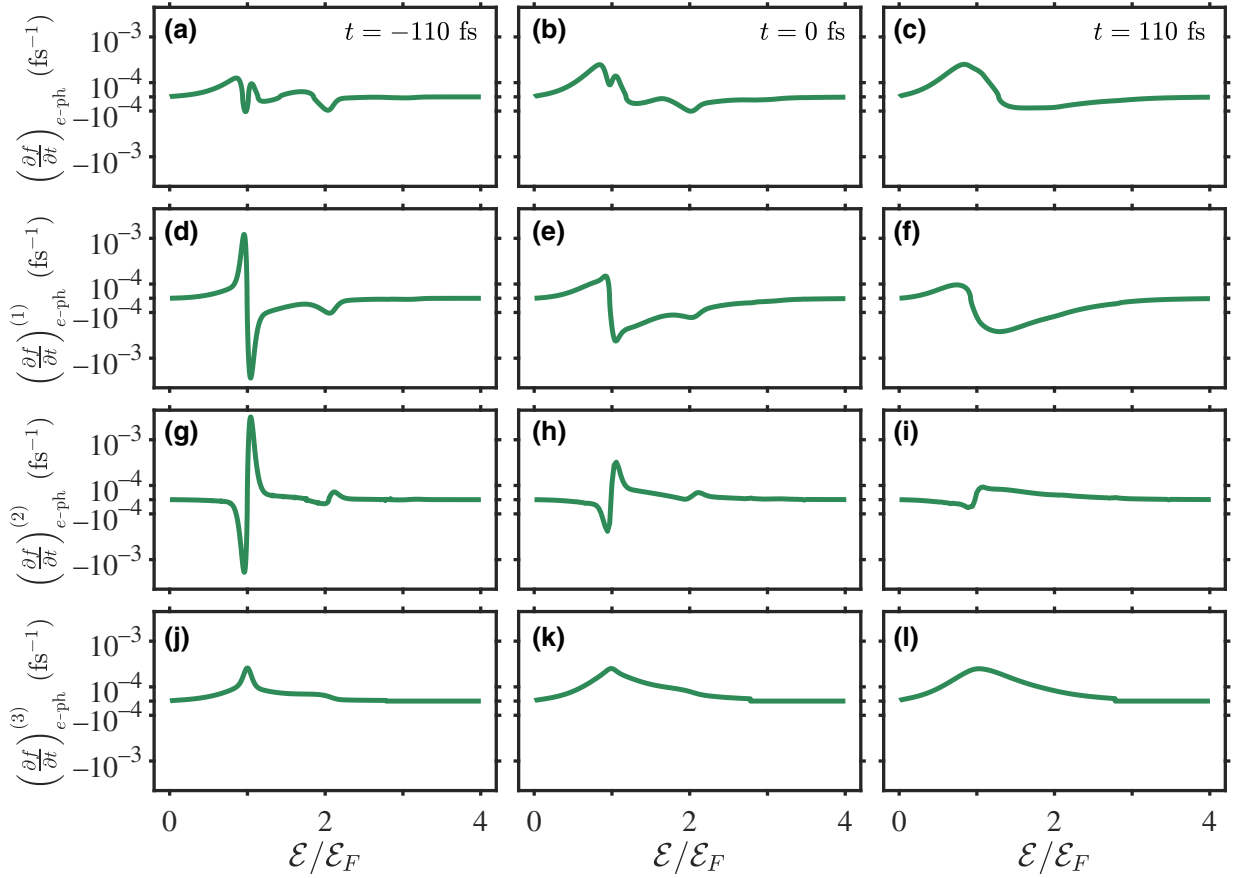
FIG. 6. (a)–(c) The e-ph collision term in Eq. (10) [the same as Figs. 2(c), 2(g), and 2(k)]. (d)–(f) The first term, (g)–(i) the second term, and (j)–(l) the third term of Eq. (A1) following illumination of ITO by a short pulse. The left column shows the various terms at the FWHM *before* the peak of the pulse ($t = -110$ fs), the middle column *at the center* of the pulse ($t = 0$ fs), and the right column at the FWHM *after* the peak of the pulse ($t = +110$ fs) as a function of $\mathcal{E}/\mathcal{E}_F$ and pulse intensity $I_{\mathrm{inc}} = 2.5$ GW/cm^2. The y axis is in symmetric log scale.

Fig. 6(j)]. For $t = 0$ and $t = 110$ fs, due to the e-e collision, the electron distribution is smeared out [see Figs. 2(e) and 2(i)]. This also smears out the peak and the step of the third term in Eq. (A1) [see Figs. 6(k) and 6(l)]. The peak and the step of $f(\mathcal{E})(1 - f(\mathcal{E}))$ then, respectively, lead to a Lorentzian dispersion shape near the Fermi energy and a dip near $\mathcal{E}_F + \hbar\omega$ in the first term of Eq. (A1), since it is proportional to the first derivative of $f(\mathcal{E})(1 - f(\mathcal{E}))$ [see Figs. 6(d)–6(f)]. Finally, since the second term of Eq. (A1) is proportional to the second derivative of $f(\mathcal{E})$ with respect to $\mathcal{E}$; it has a Lorentzian dispersion shape near $\mathcal{E}_F$ and $\mathcal{E}_F + \hbar\omega$ [see Figs. 6(g)–6(i)].

Both the first and the second terms have a Lorentzian dispersion shape near $\mathcal{E}_F$ but they are in opposite sign; the

combination of these two terms thus also has a Lorentzian dispersion shape. Combining this with the peak from the third term results in the complicated shape of $(\partial f/\partial t)_{e\text{-ph}}$ near the Fermi energy. Finally, the dip of $(\partial f/\partial t)_{e\text{-ph}}$ near $\mathcal{E}_F + \hbar\omega$ is mainly contributed by the first term in Eq. (A1) [see Figs. 6(a)–6(c)].

3. The analytical expression of the e-ph coupling coefficient $G_{e\text{-ph}}$

In this section, we provide the analytical expression of the T_e-dependent e-ph coupling coefficient $G_{e\text{-ph}}$ [Eq. (26)]. We follow the procedure mentioned in the main text, exchange the integral order, and separate the rhs of Eq. (26) into two terms, $G_{e\text{-ph}}(T_e) = G_{e\text{-ph}}^{(0)}(T_e) + G_{e\text{-ph}}^{(1)}(T_e)$:

$$G_{e\text{-ph}}^{(0)}(T_e) \approx \frac{D^2}{4\pi^3 \rho(\hbar v_{\mathrm{ph}})^4} \frac{m_e^{*2} k_B}{\hbar^3} \int_0^{\mathcal{E}_D} d\mathcal{E}_{\mathrm{ph}}(\mathcal{E}_{\mathrm{ph}})^3 \int_0^\infty d\mathcal{E} \frac{\mathcal{E}(1 + 2C\mathcal{E})}{(2k_B T_e)^2}$$

$$\times \left[(1 + 2C\mathcal{E})\mathrm{sech}^2\left(\frac{\mathcal{E} - \mu}{2k_B T_e}\right)\tanh\left(\frac{\mathcal{E} - \mu}{2k_B T_e}\right) - 4Ck_B T_e \mathrm{sech}^2\left(\frac{\mathcal{E} - \mu}{2k_B T_e}\right) \right] \tag{A2}$$

and

$$G_{e\text{-ph}}^{(1)}(T_e) \approx -\frac{D^2}{4\pi^3\rho(\hbar v_{\text{ph}})^4}\frac{m_e^{*2}k_B}{\hbar^3}\Bigg\{\int_0^{\mathcal{E}_D} d\mathcal{E}_{\text{ph}}(\mathcal{E}_{\text{ph}})^3\int_0^{\mathcal{E}^{\min}}\frac{\mathcal{E}(1+2C\mathcal{E})}{(2k_BT_e)^2}d\mathcal{E}$$

$$\times\left[(1+2C\mathcal{E})\text{sech}^2\left(\frac{\mathcal{E}-\mu}{2k_BT_e}\right)\tanh\left(\frac{\mathcal{E}-\mu}{2k_BT_e}\right) - 4Ck_BT_e\text{sech}^2\left(\frac{\mathcal{E}-\mu}{2k_BT_e}\right)\right]$$

$$+\int_0^{\mathcal{E}_D} d\mathcal{E}_{\text{ph}}(\mathcal{E}_{\text{ph}})^3\frac{\mathcal{E}^{\min}}{4k_BT_e}(1+2C\mathcal{E}^{\min})^2\text{sech}^2\left(\frac{\mathcal{E}^{\min}-\mu}{2k_BT_e}\right)\Bigg\},\tag{A3}$$

where $\mathcal{E}^{\min}(\mathcal{E}_{\text{ph}}) = 1/2C\left(\sqrt{1+C(\mathcal{E}_{\text{ph}})^2/2m_e^*v_{\text{ph}}^2}-1\right)$ is the minimum energy of an electron that can absorb or emit a phonon with energy $\mathcal{E}_{\text{ph}}$. Next, we change the variables from $\mathcal{E}$ to $x = \mathcal{E}-\mu/2k_BT_e$ and from $\mathcal{E}_{\text{ph}}$ to $x^{\min} = \mathcal{E}^{\min}-\mu/2k_BT_e$ so that $\int_0^\infty d\mathcal{E} = \int_{x_0}^\infty(2k_BT_e)dx$, $\int_0^{\mathcal{E}^{\min}} d\mathcal{E} = \int_{x_0}^{x^{\min}}(2k_BT_e)dx$ and $\int_0^{\mathcal{E}_D} d\mathcal{E}_{\text{ph}}\mathcal{E}_{\text{ph}} = \frac{1}{2}(8m_e^*v_{\text{ph}}^2)(2k_BT_e)\int_{x_0}^{x_D}dx^{\min}(1+4Ck_BT_e(x^{\min}-x_0))$, where $x_0 = -\mu/k_BT_e$, $x_D = \mathcal{E}_{\min,D}-\mu/k_BT_e$ and $\mathcal{E}_{\min,D} = 1/2C\left(\sqrt{1+C\mathcal{E}_D^2/2m_e^*v_{\text{ph}}^2}-1\right)$. Then, Eqs. (A2) and (A3) become

$$G_{e\text{-ph}}^{(0)} \approx \frac{D^2}{4\pi^3\rho(\hbar v_{\text{ph}})^4}\frac{m_e^{*2}k_B}{\hbar^3}\frac{\mathcal{E}_D^4}{4}\int_{x_0}^\infty dx\Big[(x-x_0)(1+4Ck_BT_e(x-x_0))^2\text{sech}^2(x)\tanh x$$

$$-4Ck_BT_e(x-x_0)(1+4Ck_BT_e(x-x_0))\text{sech}^2(x)\Big]\tag{A4}$$

and

$$G_{e\text{-ph}}^{(1)} \approx -\frac{D^2}{4\pi^3\rho(\hbar v_{\text{ph}})^4}\frac{m_e^{*2}k_B}{\hbar^3}(8m_e^*v_{\text{ph}}^2)^2(2k_BT_e)^2$$

$$\times\Bigg\{\frac{1}{2}\int_{x_0}^{x_D}dx^{\min}(x^{\min}-x_0)(1+2Ck_BT_e(x^{\min}-x_0))(1+4Ck_BT_e(x^{\min}-x_0))$$

$$\times\int_{x_0}^{x^{\min}}dx\Big[(x-x_0)(1+4Ck_BT_e(x-x_0))^2\text{sech}^2(x)\tanh x - 4Ck_BT_e(x-x_0)(1+4Ck_BT_e(x-x_0))\text{sech}^2(x)\Big]$$

$$+\frac{1}{4}\int_{x_0}^{x_D}dx^{\min}(x^{\min}-x_0)^2(1+2Ck_BT_e(x^{\min}-x_0))(1+4Ck_BT_e(x^{\min}-x_0))^3\text{sech}^2(x^{\min})\Bigg\}.\tag{A5}$$

To evaluate Eqs. (A4) and (A5) analytically, we define

$$g_n(x) \equiv \frac{x^n}{n!} - \ln 2\frac{x^{n-1}}{(n-1)!} - \left(-\frac{1}{2}\right)^{n-1}\text{Li}_n(-e^{-2x}),\ n\in\mathbb{Z}.\tag{A6}$$

One can verify that $g_n(x) = dg_{n+1}(x)/dx$, $g_{-2}(x) = -2\text{sech}^2(x)\tanh(x)$ and $g_{-1}(x) = \text{sech}^2(x)$. The integral in Eqs. (A4) and (A5) can thus be expressed using

$$\int_{x_0}^{x^{\min}}dx(x-x_0)^m g_n(x) = \sum_{r=0}^m\left[\frac{(-1)^r m!}{(m-r)!}(x^{\min}-x_0)^{m-r}g_{n+r+1}(x^{\min})\right] - (-1)^m g_{n+m+1}(x_0)\tag{A7}$$

and

$$
\int_{x_0}^{x_D} dx^{\min}(x^{\min} - x_0)^k \int_{x_0}^{x^{\min}} dx(x - x_0)^m g_n(x)
$$

$$
= \sum_{r=0}^{m} \sum_{s=0}^{m+k-r} \left[\frac{(-1)^{r+s} m!}{(m-r)!} \frac{(m+k-r)!}{(m+k-r-s)!} (x_D - x_0)^{m+k-r-s} g_{n+r+s+2}(x_D) \right]
$$

$$
- \sum_{r=0}^{m} \left[\frac{(-1)^{m+k} m!(m+k-r)!}{(m-r)!} g_{n+m+k+2}(x_0) \right] - (-1)^m \frac{(x_D - x_0)^{k+1}}{(k+1)!} g_{n+m+1}(x_0), \tag{A8}
$$

where m and k are positive integers.

One can then obtain the full analytical expression of $G_{e\text{-ph}}(T_e)$ by substituting Eqs. (A7)–(A8) into Eqs. (A4) and (A5). Since the full expression is too long, we do not present it here. At low electron temperatures, i.e., $k_B T_e \ll \mu$, we have $e^{-\mu/k_B T_e} \to 0$, $\ln\left(1 + e^{\mu/k_B T_e}\right) \to \mu/k_B T_e$ and $\text{Li}_2\left(-e^{-\mu/k_B T_e}\right) \to -2\left(\mu/2k_B T_e\right)^2$; then, the sum of Eqs. (A4) and (A5) reproduces Eq. (28).

APPENDIX B: THE ELECTRON-CHARGED IMPURITY COLLISION TERM

In addition to the *e-e* and *e*-ph collisions, it has been found that electron–charged-impurity ($e - \text{imp}$) interactions are another dominant scattering mechanism in thin-film ITO [50,79]. Here, we adopt the Brooks-Herring approach [52] to model the electron–charged-impurity scattering via a screened Coulomb interaction,

$$
V(\mathbf{r}) = \frac{Ze}{4\pi \varepsilon_0 \varepsilon_b |\mathbf{r} - \mathbf{R}|} e^{-q_{\text{TF}}|\mathbf{r} - \mathbf{R}|}, \tag{B1}
$$

where Z is the charge of the impurity and $\mathbf{R}$ is its position and ε_b arises from the contribution of the interband transitions to the permittivity. Following the procedure in Ref. [47] based on Fermi's golden rule, the transition rate from a state $|\mathbf{k}'\rangle$ to a state $|\mathbf{k}\rangle$ is given by

$$
W(\mathbf{k}, \mathbf{k}') = \frac{2\pi}{\hbar} |\langle \mathbf{k}| (-e)\hat{V} |\mathbf{k}'\rangle|^2 \delta(\mathcal{E}_{\mathbf{k}} - \mathcal{E}_{\mathbf{k}'}). \tag{B2}
$$

Note that it is equal to the transition rate of the reverse process $W(\mathbf{k}', \mathbf{k})$. The scattering matrix element is

$$
\langle \mathbf{k}| (-e)\hat{V} |\mathbf{k}'\rangle
$$

$$
= -\frac{1}{V} \int d^3 r \, e^{-i\mathbf{k}\cdot\mathbf{r}} \frac{Ze^2}{4\pi \varepsilon_0 \varepsilon |\mathbf{r} - \mathbf{R}|} e^{-q_{\text{TF}}|\mathbf{r} - \mathbf{R}|} e^{i\mathbf{k}'\cdot\mathbf{r}}
$$

$$
= -\frac{1}{\varepsilon_0 \varepsilon V} \frac{Ze^2}{|\mathbf{k} - \mathbf{k}'|^2 + q_{\text{TF}}^2}. \tag{B3}
$$

From the respective transition rate, the scattering term (in momentum space) in the Boltzmann Eq. (3) can then be written as

$$
\left(\frac{\partial f_{\mathbf{k}}}{\partial t}\right)_{e-\text{imp}} = N_{\text{imp}} \sum_{\mathbf{k}'} \left[W(\mathbf{k}, \mathbf{k}') f_{\mathbf{k}'}(1 - f_{\mathbf{k}}) - W(\mathbf{k}', \mathbf{k}) f_{\mathbf{k}}(1 - f_{\mathbf{k}'}) \right], \tag{B4}
$$

where N_{imp} is the total number of impurities [80]. The factor $f_{\mathbf{k}'}(1 - f_{\mathbf{k}})$ of $W(\mathbf{k}, \mathbf{k}')$ represents the probability of electron occupation in the initial state $|\mathbf{k}'\rangle$ and of electron vacancy in the final state $|\mathbf{k}\rangle$. Using $\partial f(\mathcal{E})/\partial t = 1/4\pi \int d\cos\theta_{\mathbf{k}} d\phi_{\mathbf{k}} \partial f_{\mathbf{k}}/\partial t$, we find

$$
\left(\frac{\partial f(\mathcal{E})}{\partial t}\right)_{e-\text{imp}}
$$

$$
= \frac{1}{4\pi} \int d\cos\theta_{\mathbf{k}} d\phi_{\mathbf{k}} \frac{N_{\text{imp}} V}{(2\pi)^3} \int k'^2 dk' d\cos\theta_{\mathbf{k},\mathbf{k}'} d\phi_{\mathbf{k},\mathbf{k}'}
$$

$$
\times \left(\frac{Ze^2}{\varepsilon_0 \varepsilon V}\right)^2 \frac{[f_{\mathbf{k}'}(1 - f_{\mathbf{k}}) - f_{\mathbf{k}}(1 - f_{\mathbf{k}'})] \delta(\mathcal{E}_{\mathbf{k}} - \mathcal{E}_{\mathbf{k}'})}{\left(k^2 + k'^2 - 2kk'\cos\theta_{\mathbf{k},\mathbf{k}'} + q_{\text{TF}}^2\right)^2}
$$

$$
= 0. \tag{B5}
$$

This means that the electron–charged-impurity scattering does not change the electron distribution $f(\mathcal{E})$ [26]. In fact, this result is not surprising because the initial state and the final state have the same energy in the scattering process [see Eq. (B2)]. However, the electron–charged-impurity scattering contributes to the decoherence, while the corresponding relaxation rate is nonzero and hence contributes to the damping term of the permittivity:

$$
\frac{1}{\tau_{e-\text{imp},\mathbf{k}}} = \frac{N_{\text{imp}}}{V} \frac{2\pi}{\hbar} \frac{1}{(2\pi)^3} \left(\frac{Ze^2}{\varepsilon_0 \varepsilon_b}\right)^2 \frac{\pi}{k^2} \frac{dk}{d\mathcal{E}}
$$

$$
\times \left[\left(1 - \frac{q_{\text{TF}}^2}{2k^2}\right)^2 - 1\right]^{-1}. \tag{B6}
$$

In contrast to the *e*-ph and *e-e* relaxation rates (see Ref. [81]), the $e-\text{imp}$ relaxation rate is independent of the electron distribution [26].

———

[1] G. V. Naik, J. Kim, and A. Boltasseva, Oxides and nitrides as alternative plasmonic materials in the optical range, Opt. Mater. Express **1,** 1090 (2011).

[2] M. Z. Alam, I. D. Leon, and R. W. Boyd, Large optical non-linearity of indium tin oxide in its epsilon-near-zero region, Science **116,** 795 (2016).

[3] B. T. Diroll, S. Saha, V. M. Shalaev, A. Boltasseva, and R. D. Schaller, Broadband ultrafast dynamics of refractory metals: TiN and ZrN, Adv. Opt. Mater. **8,** 2000652 (2020).

[4] Y. Yang, K. Kelley, E. Sachet, S. Campione, T. S. Luk, J.-P. Maria, M. B. Sinclair, and I. Brener, Femtosecond optical polarization switching using a cadmium oxide-based perfect absorber, Nat. Photonics **11,** 390 (2017).

[5] N. Kinsey and J. Khurgin, Nonlinear epsilon-near-zero materials explained: Opinion, Opt. Mater. Express **9,** 2793 (2019).

[6] L. Caspani, R. P. M. Kaipurath, M. Clerici, M. Ferrera, T. Roger, J. Kim, N. Kinsey, M. Pietrzyk, A. D. Falco, V. M. Shalaev, A. Boltasseva, and D. Faccio, Enhanced Nonlinear Refractive Index in ϵ-Near-Zero Materials, Phys. Rev. Lett. **116,** 233901 (2016).

[7] J. Wu, Z. T. Xie, Y. Sha, H. Y. Fu, and Q. Li, Epsilon-near-zero photonics: Infinite potentials, Photonics Res. **9,** 1616 (2021).

[8] E. Feigenbaum, K. Diest, and H. Atwater, Unity-order index change in transparent conducting oxides at visible frequencies, Nano Lett. **10,** 2111 (2010).

[9] X. Liu, J. Park, J.-H. Kang, H. Yuan, Y. Cui, H. Y. Hwang, and M. L. Brongersma, Quantification and impact of non-parabolicity of the conduction band of indium tin oxide on its plasmonic properties, Appl. Phys. Lett. **105,** 181117 (2014).

[10] A. Pradhan, R. Mundle, K. Santiago, J. Skuza, B. Xiao, K. Song, M. Bahoura, R. Cheaito, and P. E. Hopkins, Extreme tunability in aluminum doped zinc oxide plasmonic materials for near-infrared applications, Sci. Rep. **4,** 1 (2014).

[11] J. Wu, X. Liu, H. Fu, K.-C. Chang, S. Zhang, H. Y. Fu, and Q. Li, Manipulation of epsilon-near-zero wavelength for the optimization of linear and nonlinear absorption by supercritical fluid, Sci. Rep. **11,** 15936 (2021).

[12] M. Z. Alam, S. A. Schulz, J. Upham, I. D. Leon, and R. W. Boyd, Large optical nonlinearity of nanoantennas coupled to an epsilon-near-zero material, Nat. Photon. **12,** 79 (2018).

[13] J. Bohn, T. S. Luk, C. Tollerton, S. Hutchins, I. Brener, S. Horsley, W. L. Barnes, and E. Hendry, All-optical switching of an epsilon-near-zero plasmon resonance in indium tin oxide, Nat. Commun. **12,** 1017 (2021).

[14] S. Vassant, A. Archambault, F. Marquier, F. Pardo, U. Gennser, A. Cavanna, J. L. Pelouard, and J. J. Greffet, Epsilon-Near-Zero Mode for Active Optoelectronic Devices, Phys. Rev. Lett. **109,** 237401 (2012).

[15] M. Silveirinha and N. Engheta, Tunneling of Electromagnetic Energy through Subwavelength Channels and Bends Using Permittivity-Near-Zero Materials, Phys. Rev. Lett. **97,** 157403 (2006).

[16] R. Liu, Q. Cheng, T. Hand, J. J. Mock, T. J. Cui, S. A. Cummer, and D. R. Smith, Experimental Demonstration of Electromagnetic Tunneling through an Epsilon-Near-Zero Metamaterial at Microwave Frequencies, Phys. Rev. Lett. **100,** 023903 (2008).

[17] A. Alu, M. G. Silveirinha, A. Salandrino, and N. Engheta, Epsilon-near-zero metamaterials and electromagnetic sources: Tailoring the radiation phase pattern, Phys. Rev. B **75,** 155410 (2007).

[18] R. Maas, J. Parsons, N. Engheta, and A. Polman, Experimental realization of an epsilon-near-zero metamaterial at visible wavelengths, Nat. Photon. **7,** 907 (2013).

[19] P. Guo, R. D. Schaller, L. E. Ocola, B. T. Diroll, J. B. Ketterson, and R. P. H. Chang, Large optical nonlinearity of ito nanorods for sub-picosecond all-optical modulation of the full-visible spectrum, Nat. Commun. **7,** 12892 (2016).

[20] Q. Guo, Y. Cui, Y. Yao, Y. Ye, Y. Yang, X. Liu, S. Zhang, X. Liu, J. Qiu, and H. Hosono, A solution-processed ultrafast optical switch based on a nanostructured epsilon-near-zero medium, Adv. Mater. **29,** 1700754 (2017).

[21] R. Tirole, E. Galiffi, J. Dranczewski, T. Attavar, B. Tilmann, Y.-T. Wang, P. A. Huidobro, A. Alú, J. B. Pendry, S. A. Maier, S. Vezzoli, and R. Sapienza, Saturable time-varying mirror based on an ENZ material (2022).

[22] J. B. Khurgin, M. Clerici, and N. Kinsey, Fast and slow nonlinearities in epsilon-near-zero materials, Laser Photon. Rev. **15,** 2000291 (2021).

[23] P. Guo, R. D. Schaller, J. B. Ketterson, and R. P. H. Chang, Ultrafast switching of tunable infrared plasmons in indium tin oxide nanorod arrays with large absolute amplitude, Nat. Photon. **10,** 267 (2016).

[24] H. Wang, K. Du, C. Jiang, Z. Yang, L. Ren, W. Zhang, S. J. Chua, and T. Mei, Extended Drude Model for Intraband-Transition-Induced Optical Nonlinearity, Phys. Rev. Appl. **11,** 064062 (2019).

[25] J. M. Ziman, *Principles of the Theory of Solids* (Cambridge University Press, Cambridge, England, 1972).

[26] N. W. Ashcroft and N. D. Mermin, *Solid State Physics* (Brooks-Cole, Belmont, CA, USA, 1976).

[27] M. Lundstrom, *Fundamentals of Carrier Transport* (2nd ed.) (Cambridge University Press, Cambridge, England, 2000).

[28] R. H. M. Groeneveld, R. Sprik, and A. Lagendijk, Femtosecond spectroscopy of electron-electron and electron-phonon energy relaxation in Ag and Au, Phys. Rev. B **51,** 11433 (1995).

[29] N. D. Fatti, C. Voisin, M. Achermann, S. Tzortzakis, D. Christofilos, and F. Valleé, Nonequilibrium electron dynamics in noble metals, Phys. Rev. B **61,** 16956 (2000).

[30] P. Grua, J. P. Morreeuw, H. Bercegol, G. Jonusauskas, and F. Valleé, Electron kinetics and emission for metal nanoparticles exposed to intense laser pulses, Phys. Rev. B **68,** 035424 (2003).

[31] L. D. Pietanza, G. Colonna, S. Longo, and M. Capitelli, Non-equilibrium electron and phonon dynamics in metals

under femtosecond laser pulses, Eur. Phys. J. D **45**, 369 (2007).

[32] M. Kornbluth, A. Nitzan, and T. Seidman, Light-induced electronic non-equilibrium in plasmonic particles, J. Chem. Phys. **138**, 174707 (2013).

[33] J. R. M. Saavedra, A. Asenjo-García, and F. J. G. de Abajo, Hot-electron dynamics and thermalization in small metallic nanoparticles, ACS Photon. **3**, 1637 (2016).

[34] S. Franzen, Surface plasmon polaritons and screened plasma absorption in indium tin oxide compared to silver and gold, J. Phys. Chem. C **112**, 6027 (2008).

[35] E. O. Kane, Band structure of indium antimonide, J. Phys. Chem. Solids **1**, 249 (1957).

[36] T. Pisarkiewicz and A. Kolodziej, Nonparabolicity of the conduction band structure in degenerate tin dioxide, Phys. Status Solidi B **158**, K5 (1990).

[37] J. B. Khurgin and U. Levy, Generating hot carriers in plasmonic nanoparticles: When quantization does matter? ACS Photon. **7**, 547 (2020).

[38] B. Rethfeld, A. Kaiser, M. Vicanek, and G. Simon, Ultrafast dynamics of nonequilibrium electrons in metals under femtosecond laser irradiation, Phys. Rev. B **65**, 214303 (2002).

[39] Y. Dubi and Y. Sivan, "Hot electrons" in metallic nanostructures—non-thermal carriers or heating? Light: Sci. Appl. **8**, 89 (2019).

[40] L. V. Besteiro, X.-T. Kong, Z. Wang, G. Hartland, and A. O. Govorov, Understanding hot-electron generation and plasmon relaxation in metal nanocrystals: Quantum and classical mechanisms, ACS Photon. **4**, 2759 (2017).

[41] O. N. Mryasov and A. J. Freeman, Electronic band structure of indium tin oxide and criteria for transparent conducting behavior, Phys. Rev. B **64**, 233111 (2001).

[42] J.-J. Lin and Z.-Q. Li, Electronic conduction properties of indium tin oxide: Single-particle and many-body transport, J. Phys. Condens. Matter **26**, 343201 (2014).

[43] X. D. Liu, E. Y. Jiang, and D. X. Zhang, Electrical transport properties in indium tin oxide films prepared by electron-beam evaporation, J. Appl. Phys. **104**, 073711 (2008).

[44] A. M. Brown, R. Sundararaman, P. Narang, W. A. Goddard, and H. A. Atwater, Nonradiative plasmon decay and hot carrier dynamics: Effects of phonons, surfaces, and geometry, ACS Nano **10**, 957 (2016).

[45] J. Khurgin, W.-Y. Tsai, D. P. Tsai, and G. Sun, Landau damping and limit to field confinement and enhancement in plasmonic dimers, ACS Photon. **4**, 2871 (2017).

[46] For simplicity, we neglect any inhomogeneity of the local electric field in the ITO sample.

[47] D. W. Snoke, *Solid State Physics: Essential Concepts* (Pearson/Addison-Wesley, Boston, Massachusetts, 2020), 2nd ed.

[48] V. Brinzari, D. Nika, I. Damaskin, B. Cho, and G. Korotcenkov, Thermoelectric properties of nano-granular indium–tin-oxide within modified electron filtering model with chemisorption-type potential barriers, Phys. E **81**, 49 (2016).

[49] This value of the deformation potential is obtained by fitting the ITO permittivity (at room temperature) calculated by the Lindhard formula [82] with that measured experimentally [24].

[50] H. Wang, K. Du, R. Liu, X. Dai, W. Zhang, S. J. Chua, and T. Mei, Role of hot electron scattering in epsilon-near-zero optical nonlinearity, Nanophotonics **9**, 4287 (2020).

[51] D. Kim, A. Aydin, A. Daza, K. N. Avanaki, J. Keski-Rahkonen, and E. J. Heller, Coherent electron dynamics in thermal lattice vibrations (2020).

[52] B. K. Ridley, *Quantum Processes in Semiconductors* (Oxford University Press, Oxford, 2013), 5th ed.

[53] P. Coleman, *Introduction to Many Body Physics* (Cambridge University Press, Cambridge, Massachusetts, 2015).

[54] A. N. Smith and P. M. Norris, Influence of intraband transitions on the electron thermoreflectance response of metals, Appl. Phys. Lett **78**, 1240 (2001).

[55] From Eq. (15), one can deduce that the Thomas-Fermi wave vector is proportional to the square root of the eDOS at the Fermi energy [26]. Therefore, compared with the case of $C = 0$, q_{TF} is larger by a factor of $(1 + C\mu(T_e))^{1/4}(1 + 2C\mathcal{E}_F)^{1/2}$ and k_F is larger by a factor of $(1 + C\mu(T_e))^{1/2}$. Together with the factor $(1 + 2C\mu(T_e))^3$ coming from the increase of eDOS, the e-e thermalization rate increases by a factor of approximately $(1 + 2C\mu(T_e))^{3/2}(1 + C\mu(T_e))^{-5/4}$.

[56] Note that the term $(\mathcal{E} - \mu(T_e))$ in Eq. (18) should not be replaced by $\hbar\omega/2$, since it involves all possible electron states, rather than only those excited from the Fermi energy by photon absorption.

[57] The Thomas-Fermi wave vector is proportional to the square root of the eDOS at the Fermi energy [26]; thus, it decreases with the electron density.

[58] Y. Sivan and Y. Dubi, Theory of "hot" photoluminescence from Drude metals, ACS Nano **15**, 8724 (2021).

[59] T. Stoll, P. Maioli, A. Crut, N. D. Fatti, and F. Vallée, Advances in femto-nano-optics: Ultrafast nonlinearity of metal nanoparticles, Eur. Phys. J. B **87**, 260 (2014).

[60] T. Yagi, K. Tamano, Y. Sato, N. Taketoshi, T. Baba, and Y. Shigesato, Analysis on thermal properties of tin doped indium oxide films by picosecond thermoreflectance measurement, J. Vac. Sci. Technol. A **23**, 1180 (2005).

[61] S. I. Anisimov, B. L. Kapeilovich, and T. I. Perelman, Electron emission from metal surfaces exposed to ultrashort laser pulses, Sov. Phys. JETP **39**, 375 (1974).

[62] This is reminiscent of what happens in semiconductors [26, 83,84].

[63] A. Sommerfeld, Zur Elektronentheorie der Metalle auf Grund der Fermischen Statistik, Z. Phys. **47**, 1 (1928).

[64] Due to nonparabolicity, the dependence of γ_e on the electron density is not straightforward. In contrast, in its absence, γ_e reduces to the familiar expression $\gamma_e = \pi^2 n_e k_B^2 / 2\mathcal{E}_F$.

[65] Z. Lin, L. V. Zhigilei, and V. Celli, Electron-phonon coupling and electron heat capacity of metals under conditions of strong electron-phonon non-equilibrium, Phys. Rev. B **77**, 075133 (2008).

[66] P. B. Allen, Theory of Thermal Relaxation of Electrons in Metals, Phys. Rev. Lett. **59**, 1460 (1987).

[67] For Au, Eq. (27) becomes $G_{e\text{-ph}}^{(\text{Au})} = D^2 m_e k_B \mathcal{E}_D^4 / 16(\pi\hbar)^3 \rho(\hbar v_{\text{ph}})^4$; with the known parameters for Au [29] (viz. the deformation potential $D = 19.3$ eV, Debye energy $\mathcal{E}_D = 0.014$ eV, mass density $\rho = 19.3 \times 10^3$ Kg/m^3, and

phonon velocity $v_{ph} = 3240$ m/s), one obtains the above value.

[68] The same reasoning explains why an increase in the phonon temperature does not have a significant effect [see Eq. (26)].

[69] C. Voisin, D. Christofilos, P. A. Loukakos, N. D. Fatti, F. Valleé, J. Lermé, M. Gaudry, E. Cottancin, M. Pellarin, and M. Broyer, Ultrafast electron-electron scattering and energy exchanges in noble-metal nanoparticles, Phys. Rev. B **69,** 195416 (2004).

[70] Y. Sivan and Y. Dubi, Recent developments in plasmon-assisted photocatalysis—a personal perspective, Appl. Phys. Lett. **117,** 130501 (2020).

[71] T. Haug, P. Klemm, S. Bange, and J. M. Lupton, Hot-Electron Intraband Luminescence from Single Hot Spots in Noble-Metal Nanoparticle Films, Phys. Rev. Lett. **115,** 067403 (2015).

[72] R. B. Wilson and S. Coh, Parametric dependence of hot electron relaxation timescales on electron-electron and electron-phonon interaction strengths, Commun. Phys. **3,** 035424 (2020).

[73] R. W. Schoenlein, W. Z. Lin, J. G. Fujimoto, and G. L. Eesley, Femtosecond Studies of Nonequilibrium Electronic Processes in Metals, Phys. Rev. Lett. **58,** 1680 (1987).

[74] E. Carpene, Ultrafast laser irradiation of metals: Beyond the two-temperature model, Phys. Rev. B **74,** 024301 (2006).

[75] G. D. Valle, M. Conforti, S. Longhi, G. Cerullo, and D. Brida, Real-time optical mapping of the dynamics of non-thermal electrons in thin gold films, Phys. Rev. B **86,** 155139 (2012).

[76] Y. Sivan, I. W. Un, and Y. Dubi, Assistance of plasmonic nanostructures to photocatalysis—just a regular heat source, Faraday Discuss. **214,** 215 (2019).

[77] J. Baxter, A. Pérez-Casanova, L. Cortes-Herrera, A. C. Lesina, I. D. Leon, and L. Ramunno, Understanding the nonlinear optical response of epsilon near zero materials in the time-domain, arXiv:2110.14806v1 [physics.optics] (2021).

[78] This explains why the polar integral in Eq. (9) is nonzero only when $q \lesssim 2k$.

[79] H.-C. Lee, Electron scattering mechanisms in indium–tin-oxide thin films prepared at the various process conditions, Appl. Surf. Sci. **252,** 3428 (2006).

[80] In Eq. (B5), we can see that $\partial f / \partial t$ is proportional to $N_{imp}V/V^2 = N_{imp}/V$, the impurity density.

[81] S. Sarkar, I. W. Un, and Y. Sivan, The electronic and thermal response of low electron density Drude materials to ultrafast optical illumination (2022), ArXiv:2207.14528v1.

[82] G. Grosso and G. Parravicini, *Solid State Physics* (Academic Press, London, 2014), 2nd ed.

[83] S. M. Sze, in *Physics of Semiconductor Devices* (John Wiley & Sons, Ltd, 2006), p. 5.

[84] S. Sarkar, I. W. Un, Y. Sivan, and Y. Dubi, Theory of non-equilibrium "hot" carriers in direct band-gap semiconductors under continuous illumination, New J. Phys. **24,** 053008 (2022).